



2006-07-06

A Search for Low-Amplitude Variability Among Population I Main Sequence Stars

Michael Benjamin Rose
Brigham Young University - Provo

Follow this and additional works at: <https://scholarsarchive.byu.edu/etd>

 Part of the [Astrophysics and Astronomy Commons](#), and the [Physics Commons](#)

BYU ScholarsArchive Citation

Rose, Michael Benjamin, "A Search for Low-Amplitude Variability Among Population I Main Sequence Stars" (2006). *All Theses and Dissertations*. 915.

<https://scholarsarchive.byu.edu/etd/915>

This Thesis is brought to you for free and open access by BYU ScholarsArchive. It has been accepted for inclusion in All Theses and Dissertations by an authorized administrator of BYU ScholarsArchive. For more information, please contact scholarsarchive@byu.edu, ellen_amatangelo@byu.edu.

A SEARCH FOR LOW-AMPLITUDE VARIABILITY AMONG
POPULATION I MAIN SEQUENCE STARS

by

Michael Benjamin Rose

A thesis submitted to the faculty of

Brigham Young University

in partial fulfillment of the requirements for the degree of

Master of Science

Department of Physics and Astronomy

Brigham Young University

July 2006

Copyright © 2006 Michael Benjamin Rose

All Rights Reserved

BRIGHAM YOUNG UNIVERSITY

GRADUATE COMMITTEE APPROVAL

of a thesis submitted by

Michael Benjamin Rose

This thesis has been read by each member of the following graduate committee and by majority vote has been found to be satisfactory.

Date

Eric G. Hintz, Chair

Date

Benjamin J. Taylor

Date

Bryan G. Peterson

BRIGHAM YOUNG UNIVERSITY

As chair of the candidate's graduate committee, I have read the thesis of Michael Benjamin Rose in its final form and have found that (1) its format, citations, and bibliographical style are consistent and acceptable and fulfill university and department style requirements; (2) its illustrative materials including figures, tables, and charts are in place; and (3) the final manuscript is satisfactory to the graduate committee and is ready for submission to the university library.

Date

Eric G. Hintz
Chair, Graduate Committee

Accepted for the Department

Ross L. Spencer, Graduate Coordinator
Department of Physics and Astronomy

Accepted for the College

Thomas W. Sederberg, Associate Dean
College of Physical and Mathematical Sciences

ABSTRACT

A SEARCH FOR LOW-AMPLITUDE VARIABILITY AMONG POPULATION I MAIN SEQUENCE STARS

Michael Benjamin Rose

Department of Physics and Astronomy

Master of Science

The detection of variable stars in open clusters is an essential component of testing stellar structure and evolution theories. The ability to detect low-amplitude variability among cluster members is directly related to the quality of the photometric results. Point Spread Function (PSF) fitting is the best method available for measuring accurate magnitudes within crowded fields of stars, while high-precision differential photometry is the preferred technique for removing the effects of atmospheric extinction and variable seeing. In the search for new variable stars among hundreds or thousands of stars, the Robust Median Statistic (RoMS) is proven more effective for finding low-amplitude variables than the traditional error curve approach. A reputable computer program called DAOPHOT was used to perform PSF fitting, whereas programs, CLUSTER and RoMS, were created to carry out high-precision differential photometry and calculate the RoMS, respectively, on the open clusters NGC 225, NGC 559, NGC 6811, NGC 6940, NGC 7142, and NGC 7160. Twenty-two

new variables and eighty-seven suspected variable stars were discovered, and time-series data of the new variables are presented.

ACKNOWLEDGMENTS

I would like to thank Dr. Eric Hintz for his wonderful insights and instruction over the past five years. Without his guidance, patience, and vision this project would have never been possible. I would also like to thank Dr. Benjamin Taylor for helping me understand the powerful capabilities of statistical analysis, and explaining so many concepts over and over until they made sense. In addition, I would like to thank Dr. Bryan Peterson, Maureen Hintz, Mike Joner, and Jacob Albretsen for their proofreading skills as well as the many corrections and constructive suggestions that made this thesis so much better. I would like to thank Ted Maxwell for his help in understanding how to use DAOPHOT and the many scripts that he has written to aid in the photometric analysis process. I would like to acknowledge the financial support of the Brigham Young University Department of Physics and Astronomy and the use of the 1.8 m Plaskett Telescope at the Dominion Astrophysical Observatory, Herzberg Institute of Astrophysics, National Research Council of Canada. Finally, I would like to thank my wife, Kathy, and daughter, Taylor, for their support and understanding when I needed to devote so much of my time to finish this project.

Contents

Acknowledgments	vii
Table of Contents	viii
List of Tables	xi
List of Figures	xii
1 Introduction and Background	1
1.1 Stellar Clusters	1
1.1.1 Globular Clusters and Stellar Populations	2
1.1.2 Open Clusters	3
1.2 Hertzsprung-Russell Diagram	4
1.2.1 Key Areas in the CM-diagram	5
1.2.2 Observed CM-diagram Differences	8
1.2.3 Theoretical Models	9
1.3 Variable Stars	10
1.3.1 Pulsating Variables	12
1.4 The Problem and Objectives	15
1.4.1 Selected Open Clusters	16
1.4.2 Current Research	17
2 Observations and Reductions	18
2.1 Photometric Observations	18
2.1.1 Orson Pratt Observatory	18
2.1.2 Dominion Astrophysical Observatory	19
2.1.3 Nominal Exposure Lengths	19
2.2 Image Reductions	22

2.2.1	Calibration Frames	23
2.2.2	Important CCD Properties	24
2.2.3	Image Processing Steps	26
3	Photometric Methods	29
3.1	Obtaining Instrumental Magnitudes	29
3.1.1	Digital Aperture Photometry	29
3.1.2	Point Spread Function Fitting	30
3.2	Differential Photometry	31
3.2.1	Applying Differential Photometry	33
3.2.2	Differential Photometry Software	34
3.2.3	Outline of Procedures	35
3.3	Robust Median Statistic	37
3.3.1	Defining the RoMS	37
3.3.2	Defining the Analytical Function	38
3.3.3	RoMS Software	40
3.3.4	Outline of Procedures	41
4	Results and Analysis	42
4.1	Statistical Distributions	42
4.2	Potential Variable Stars	43
4.3	Time-series Plots	59
5	Conclusions	72
A	User's Guide to CLUSTER	74
A.1	Expected Input File	74
A.2	A Typical Run of CLUSTER	75
A.3	Output Files	76
B	User's Guide to ROMS	80

List of Tables

1.1	Key features in the CM-diagram	10
1.2	Defining characteristics for pulsators	14
1.3	Open clusters observed in this study	17
2.1	Photometric observations of open clusters	20
2.2	Universal table of apparent visual magnitudes	22
2.3	Nominal exposure lengths on the 0.4 m David Derrick Telescope	23
2.4	Summary of CCD properties	26
4.1	Potential variable stars in NGC 225	47
4.2	Potential variable stars in NGC 559	48
4.3	Potential variable stars in NGC 6811	49
4.4	Potential variable stars in NGC 6940	50
4.5	Potential variable stars in NGC 7142	51
4.6	Potential variable stars in NGC 7160	52

List of Figures

1.1	Color image of the globular cluster M3	4
1.2	Color image of the open cluster NGC 4755	4
1.3	Color-magnitude diagram with Y^2 isochrones and principal sequences marked	7
1.4	Color-magnitude diagram of the globular cluster M3	9
1.5	Color-magnitude diagram of the open cluster NGC 4755	9
1.6	Color-magnitude diagram of pulsating variables and the instability strip	13
2.1	Color images of Open Clusters: NGC 225, NGC 559, NGC 6811, NGC 6940, NGC 7142, and NGC 7160	28
3.1	Schematic drawing of stellar image with marked aperture and sky annuli	31
3.2	Schematic drawing of overlapping stellar images with marked apertures	31
3.3	PSF model of the intensity distribution of a stellar point source on a CCD	32
3.4	Radial plot of a stellar PSF and profile fit	32
3.5	Air mass-magnitude diagram showing the effect of atmospheric extinction	34
3.6	Plot of the average value of the ensemble versus time	34
3.7	Magnitude-error diagram of the cluster NGC 559	36
3.8	Semi-log magnitude-error diagram of the cluster NGC 559	38
3.9	Magnitude-error diagram of the cluster NGC 559 with the RoMS an- alytical function	40
4.1	Histogram of the RoMS values for NGC 225	44
4.2	Histogram of the RoMS values for NGC 559	44
4.3	Histogram of the RoMS values for NGC 6811	44
4.4	Histogram of the RoMS values for NGC 6940	44
4.5	Histogram of the RoMS values for NGC 7142	45
4.6	Histogram of the RoMS values for NGC 7160	45

4.7	Histogram of the RoMS values for all potential variables	45
4.8	ME-diagram of NGC 6940 with new variables marked	46
4.9	Finder chart for potential variables in NGC 225	53
4.10	Finder chart for potential variables in NGC 559	54
4.11	Finder chart for potential variables in NGC 6811	55
4.12	Finder chart for potential variables in NGC 6811	56
4.13	Finder chart for potential variables in NGC 7142	57
4.14	Finder chart for potential variables in NGC 7160	58
4.15	Time-series plot of new variable star 35 in NGC 225	60
4.16	Time-series plot of potential variable star 42 in NGC 225	60
4.17	Time-series plot of potential variable star 66 in NGC 225	61
4.18	Time-series plot of potential variable star 68 in NGC 225	61
4.19	Time-series plot of new variable star 8 and nearby stable star 7 in NGC 6811	63
4.20	Time-series plot of potential variable star 30 in NGC 6811	64
4.21	Time-series plot of potential variable star 62 in NGC 6811	64
4.22	Time-series plot of new variable star 35 in NGC 6811	65
4.23	Time-series plot of new variable star 41 in NGC 6811	66
4.24	Time-series plot of new variable star 10 in NGC 6940	66
4.25	Time-series plot of new variable star 32 in NGC 6940	67
4.26	Time-series plot of new variable star 91 in NGC 6940	67
4.27	Time-series plot of new variable star 99 in NGC 6940	68
4.28	Time-series plot of new variable star 192 in NGC 6940	68
4.29	Time-series plot of new variable star 198 in NGC 6940	69
4.30	Time-series plot of new variable star 214 in NGC 6940	69
4.31	Time-series plot of new variable star 262 in NGC 6940	70
4.32	Time-series plot of new variable star 34 in NGC 7142	71
5.1	Color-magnitude diagram of the cluster NGC 6940	73
A.1	Sample input file for CLUSTER	75

A.2	Sample error file from CLUSTER	77
A.3	Sample magnitude file from CLUSTER	78
A.4	Sample log file from CLUSTER	79
B.1	Sample RoMS output file	81

Chapter 1

Introduction and Background

1.1 Stellar Clusters

Stellar clusters play a fundamental role in our understanding of the Universe. Some important discoveries from the study of clusters include: the structure and evolution of galaxies, the formation and life cycle of stars, and the location of the Solar System in the Milky Way. Clusters are created from the process of cascading fragmentation during the collapse of a molecular cloud. As a result, three general characteristics arise: every member of the cluster was formed (1) from the same cloud, (2) at the same time, and (3) with approximately identical compositions.

In addition, the size of a typical cluster is relatively small compared to its distance from us. Thus, another characteristic emerges: (4) each member lies at approximately the same distance. This means that the difference between absolute and apparent magnitude will be the same for every star in the cluster. Furthermore, the differences in evolutionary states between the various stars in the cluster are due solely to their initial masses.

For the purpose of understanding the goals of this thesis, a brief overview of globular clusters and stellar populations is given in § 1.1.1, followed by a detailed treatment of open clusters in § 1.1.2. Section 1.2 provides an introduction to the tools inherent to the Hertzsprung-Russell diagram for the study of the evolutionary state of open clusters. Section 1.3 is a brief discussion of the variable stars commonly found in open clusters and Section 1.4 brings all of these concepts together, explains the problem at hand, and offers the objective of this thesis. It will also be shown that the characteristics mentioned above play a vital role in this study.

1.1.1 Globular Clusters and Stellar Populations

Clusters are separated into two distinct classes: globular and open. Globular clusters (hereafter *globulars*) are roughly spherical in nature, tightly bound by gravity, free of diffuse gas and dust, and dominated by luminous red stars (see Figure 1.1). The overabundance of red stars and lack of bright blue stars in these systems prompted the study and classification of stellar populations: Population I and Population II. Population I contains luminous blue stars interlaced with dust and gas, while Population II is dominated by luminous red stars and devoid of gas and dust.

From detailed spectral analysis, Population II stars are found to be considerably deficient in all elements heavier than helium (referred to as *metal-poor*), whereas Population I stars have a greater percentage of heavy elements (or *metal-rich*). This difference in heavy element abundances is attributed to a difference in age, with Population II stars forming noticeably earlier than Population I stars. As a result, it is presumed that globulars, being made up of Population II stars, were the first parts of the Galaxy to form.

Furthermore, the absolute age of the oldest globulars provides an estimate of the age of the Milky Way and a lower limit to the age of the Universe. Recent published values from the literature include 11.5 ± 1.3 Gyr (Chaboyer et al. 1998) and 12.5 ± 0.7 Gyr (McNamara et al. 2004).

Globulars are located primarily in the Galactic halo in a nearly symmetrical distribution about the center of the Galaxy. From this distribution, Harlow Shapley reasoned that the Sun is located ~ 15 kpc from the center of the Milky Way (Binney & Merrifield 1998). In 1985, the International Astronomical Union (IAU) voted the standard solar galactocentric distance to be 8.5 ± 1.1 kpc (Kerr & Lynden-Bell 1986), whereas more recent measurements yield 7.0 ± 0.8 kpc (Merrifield 1992). The discrepancy in Shapley's measurements is attributed to a non-accounting of interstellar extinction (the dimming of light by absorption and scattering), which was brought forward later by Trumpler (1930).

1.1.2 Open Clusters

Open clusters exhibit very limited symmetry in their structure and lack the central concentration characteristic found in globulars (see Figure 1.2). They are loosely bound by gravity, cluttered by gas and dust, recognized by their large number of bright blue stars, and known as the stellar nurseries of the Milky Way. From these characteristics and the previous discussion of stellar populations, it is inferred that open clusters are made up of Population I stars. Since open clusters tend to be metal-rich, variations in heavy element abundance will likely have a negligible impact on the interpretation of their properties; however this is not the case for globulars.

Although open clusters are intrinsically younger and smaller than most globulars, they span a wide range in size, age, and morphology—all of which are dependent upon such factors as membership, density, and location in the Galaxy. Open cluster membership can vary from a few dozen or so stars (known as *associations*) up to thousands of stars, while their densities range anywhere from the field-star density, ~ 0.1 stars pc^{-3} , up to $\sim 10^3$ stars pc^{-3} (Binney & Merrifield 1998). Typical values of age range from ~ 1 Myr for young clusters (i.e. NGC 2024, NGC 2068, and NGC 2071, Lada et al. 1991) to ~ 8 Gyr for atypical old clusters, such as NGC 188 and NGC 2682 (Becker & Fenkart 1971).

Open clusters are usually located in the plane or disk of the Galaxy, thus their spatial distribution provides a useful probe of the structure of the Galactic disk. The older clusters, which tend to reside furthest from the Galactic plane, outline the kinematics of the outer Galaxy, while the very young associations, which precipitate within the disk, trace the spiral structure of the Galaxy. In addition, the very young clusters are used to study star formation and its recent history, as well as define the initial mass and luminosity functions (Friel 1995).

As a result of their position in the Galactic disk, many open clusters tend to be heavily concealed by dust, thus only nearby examples can be detected. Since these clusters are relatively close to the Sun, their distances can be measured directly by



Figure 1.1: Color photo of the globular cluster M3. M3 exhibits the compact, spherical nature of most globulars as well as the luminous red giants. [Image courtesy of Kafka & Honeycutt (2006) NOAO/AURA/NSF, WIYN Consortium, Inc.]



Figure 1.2: Color photo of the open cluster NGC 4755. NGC 4755 shows the open nature of open clusters with the bright blue stars. [Image courtesy of NOAO/AURA/NSF, WIYN Consortium, Inc.]

the trigonometric parallax method. The distance to the nearby Hyades cluster was of considerable, historical significance because the cluster contains specific spectral-types of stars that could not be calibrated locally. Moreover, the distance to the Hyades became the foundation for all Galactic and extragalactic distance measurements (Binney & Merrifield 1998).

1.2 Hertzsprung-Russell Diagram

The Hertzsprung-Russell diagram (HR-diagram), developed independently by Ejnar Hertzsprung in 1911 and Henry Norris Russell in 1913, exhibits an extraordinary correlation among two stellar properties: absolute visual magnitude and spectral type. As a result, the HR-diagram has played a key role in our understanding of stellar evolution. The HR-diagram is both a profound tool for exploring the history of the Galaxy and the most compelling test of the theory of stellar evolution.

Variations of the HR-diagram are more commonly used today, in which the discrete spectral type has been replaced by a continuous coordinate. From an observational perspective, the most useful form is the *color-magnitude diagram* (CM-diagram), which is either a plot of color versus absolute magnitude (for stars with known distances) or apparent magnitude (for stars at the same distance). The second form, convenient for theoretical work, is the *theoretical CM-diagram*, which is a plot of effective temperature, T_{eff} , versus luminosity, $\log(L/L_{\odot})$. The difficulty lies in developing a quantitative correspondence between a CM-diagram and the theoretical CM-diagram.

1.2.1 Key Areas in the CM-diagram

In an observed CM-diagram, the stars are not randomly scattered, but rather form tightly bound bands or *sequences*. From the theory of stellar structure and evolution, it is learned that these sequences represent a particular stage of a star's evolutionary path. In other words, the location of a star in a CM-diagram is dependent upon the structure of the star as well as the rate at which it is generating energy by nuclear fusion in its core.

Main Sequence

Of the concentrations of stars in the CM-diagram, the most important is the *main sequence* (MS), which stretches from luminous, hot, blue, O stars to faint, cool, red, M stars (see Figure 1.3). Main sequence stars are dwarfs (MK luminosity class V) that are burning H to He in their cores. Additionally, the main sequence is where stars spend the greater portion of their lives. The position of a star on the main sequence depends on its mass: more massive stars to the left and less massive stars to the right. The *zero-age main sequence* (ZAMS) is a theoretical main sequence for stars of a hypothetical population with age zero (see Figure 1.3).

Subgiant & Red Giant Branches

As a star reaches the end of its H-burning phase, it evolves up and away from the ZAMS onto the *subgiant branch* (SGB; see Figures 1.3 and 1.4). On the subgiant branch, stars are burning H to He in a shell rather than in their cores, but have not developed fully convective envelopes. The *red giant branch* (RGB) connects to the subgiant branch at $B-V \simeq 1$ and turns sharply upwards in the CM-diagram (see Figure 1.3). In this region, the stars are burning H to He in a shell and have developed fully convective envelopes. These stars will cool and their atmospheres will expand as they climb the red giant branch. The red giant branch ends abruptly at the He-flash, which occurs when the core collapses and ignites the burning of He.

Turnoff Point

The intersection of the main sequence and subgiant branch is defined as the *turnoff point* (TO)—the point at which the ridge-line of the MS/SGB runs vertically up the CM-diagram (see Figures 1.3, 1.4, and 1.5). The stars just above the turnoff point are evolving off the main sequence together, which suggests that these stars have essentially identical ages (or MS-lifetimes). As a result, the location of the turnoff point is used to measure the age of a cluster.

Blue Stragglers

In some clusters, a group of stars is found above the turnoff point, yet still on the main sequence. These unusual stars are called *blue stragglers* (BS), since they appear to have found a new source of hydrogen, or fountain of youth, to sustain life on the main sequence (see Figure 1.4). A few possible explanations to this behavior include: merger with a close companion, mass exchange with a binary companion, and some process of internal mixing or combination of the above.

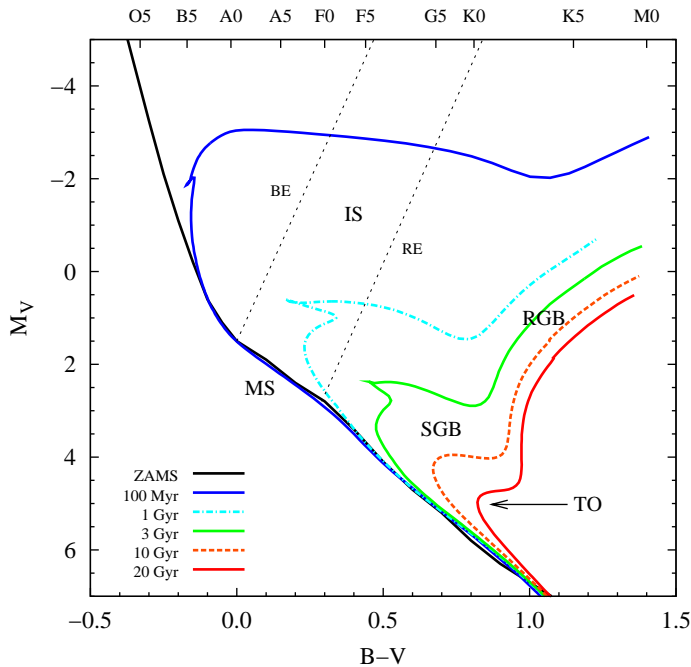


Figure 1.3: CM-diagram that includes the principal sequences and theoretically calculated isochrones. The isochrones show how a stellar population with $Z = 0.02$ and $Y = 0.27$ (near solar content) evolves away from the *zero-age main sequence* (ZAMS). The *turnoff point* (TO) is only labeled for one isochrone but applies to corresponding areas of the other isochrones. [Isochrones from the calculations of Demarque et al. (2004), ZAMS and Martin & Kirkpatrick (MK) spectral types from data published in Schmidt-Kaler (1982), and *instability strip* (IS) from data published in Paunzen et al. (2004).]

Instability Strip

There exists a nearly vertical region, in the CM-diagram, where stars are found to pulsate (see Figure 1.3). This *instability strip* (IS) is defined as the region where the κ mechanism drives pulsation. In brief, the ionization of He II \rightarrow He III, from radiation, causes the opacity (κ) of the ionized layer to increase with temperature at specific radii within the star—the result is an expanding and contracting atmosphere.

The *blue edge* (BE) of the instability strip is the result of the He II ionization layer being too close to the surface where there is not enough mass to drive the pulsation. The *red edge* (RE) is due to the ionization layer residing in a convective region deep within the star where the dominant method of energy transport is convection, not radiation. Figure 1.3 uses these edges to define the classical instability strip, while Table 1.1 presents a summary of the key areas of the CM-diagram.

1.2.2 Observed CM-diagram Differences

From the previous discussion of stellar populations, it was determined that globulars and open clusters are made up of Population II and I stars, respectively. Thus, it is no surprise that there are noticeable differences in their CM-diagrams – see Figures 1.4 and 1.5. As a result of their old age, globulars, such as M3 in Figure 1.4, exhibit a short main sequence, a red turnoff point, well-defined subgiant and red giant branches, and a pronounced *horizontal branch* (HB). Stars on the horizontal branch are burning He in their cores (similar to the H-burning MS), and tend to lie within the instability strip—making them RR Lyrae variables (see §1.3).

On the other hand, young open clusters, such as NGC 4755 in Figure 1.5, feature an extensive main sequence that contains high-mass stars, very few evolved subgiants, and lack red giant and horizontal branches. Towards the bottom of the main sequence of young open clusters, we frequently find that the sequence becomes broader with an increased scattering of stars on the red side. In older clusters, the apparent broadening of the faint end of the main sequence is due to large uncertainties in the magnitudes of the faintest stars, which propagates to a very large error in the color ($B - V$).

Moreover, the width of NGC 4755’s main sequence is too large to be completely attributed to observational errors, and cannot be the result of random extinction. We would expect such variable reddening to affect the colors of some of the brighter stars; however, the upper part of the main sequence appears to be well-defined. The broadening of the main sequence at low luminosities is actually a consequence of the cluster’s youth: low-mass stars take longer to contract onto the main sequence from the Hayashi limit (on the extreme right of the CM-diagram) than higher-mass stars. Stars observed in their transition to the main sequence are called *pre-main-sequence* (PMS) stars (see Figure 1.5).

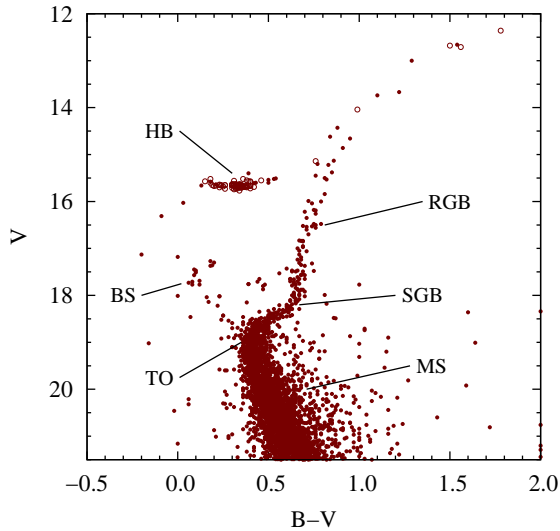


Figure 1.4: The CM-diagram of the old globular cluster M3. Known variable stars are shown as open circles and the principle sequences are noted. [From data published in Buonanno et al. (1994).]

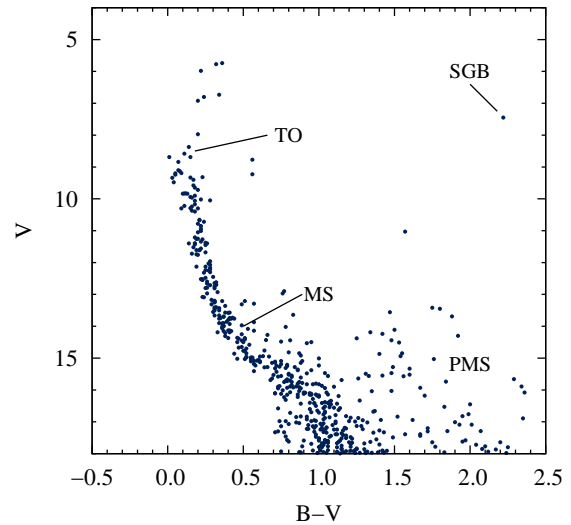


Figure 1.5: The CM-diagram of the young open cluster NGC 4755. Note the MS extending well into the blue region and lack of other sequences found in M3. [From data published in Sagar & Cannon (1995) and Dachs & Kaiser (1984).]

1.2.3 Theoretical Models

Computer models, built upon stellar evolution theory, are used to calculate the evolutionary paths of stars of various masses, in which all stars have the same chemical composition as a given cluster. For each time step, the colors and luminosities are calculated, then when a particular time step is plotted in a CM-diagram, the curve connecting all the stars is called an *isochrone*, from the Greek word for “same time” (Binney & Merrifield 1998). The isochrone represents a snapshot of the properties of the stellar population (or cluster) at a specific age.

Figure 1.3 presents a CM-diagram of five isochrones, from the calculations of Demarque et al. (2004), each with chemical composition of $X = 0.71$, $Y = 0.27$, and $Z = 0.02$, which represent the initial fraction of total mass of hydrogen, helium, and all other elements, respectively; this metal abundance corresponds to the solar content. Additionally, the ages of these snapshots, which range from 100 Myr to 20 Gyr, were chosen to portray the effect that age has on a population of stars—as

Table 1.1. Key features in the CM-diagram

Features	Physical significance
Main sequence (MS)	Core H burning
Zero-age main sequence (ZAMS)	Theoretical zero-age of stars
Subgiant branch (SGB)	Transition from core to shell H burning
Red giant branch (RGB)	Shell H burning
Turnoff point (TO)	Used to determine age of stars
Blue stragglers (BS)	Additional source of H
Instability strip (IS)	He II ionization zone gives rise to variables
Horizontal branch (HB)	Core He burning

References. — Parts taken from Binney & Merrifield (1998).

a cluster ages, fewer and fewer stars remain on the main sequence. Hence, the main sequence becomes shorter while the other sequences become more defined.

1.3 Variable Stars

The probability of discovering many types of variables in this study requires that a discussion of variable stars include a brief description of the four main classes of variables. However, the primary focus of this research is to discover and study a single class of variables, namely pulsating variable stars, which are subsequently discussed in detail.

Variable stars play an important role in astronomy. In the early 1920's, Edwin Hubble used pulsating variable stars—called Cepheids—to measure the distance to the great spiral nebula in Andromeda. He found that the Cepheids in Andromeda were so much farther away than those in our Milky Way that Andromeda must be a separate galaxy. This discovery changed our perception of the size of the Universe, settled the long debate over the nature of spiral nebulae, confirmed Harlow Shapley's model of the galaxy, and showed how pulsating variables serve as standard candles to measure cosmic distances (Binney & Merrifield 1998).

All stars are variable, to one degree or another, because stars tend to oscillate and these oscillations result in variations in luminosity. However, a star is only termed *variable* when it demonstrates a change in brightness greater than 0.001 mag. This change in luminosity, used to define the classification system of variable stars, allows all variables to be separated into two groups: intrinsic and extrinsic. Intrinsic, meaning *interior to the system*, variables show variation in brightness due to some change in the physical properties of the system while extrinsic, meaning *exterior to the system*, variables show light variation due to one star passing in front of another in our line of sight or the effects of stellar rotation.

As a result, the intrinsic group is separated into two classes, namely *pulsating* and *eruptive* (or cataclysmic), while the extrinsic group is divided into *eclipsing* and *rotating*. Eruptive variables, as the name implies, are stars that experience violent explosions due to thermonuclear reactions either on the surface or deep within the star. Examples of eruptive variables include supernovae, novae, and recurrent novae.

Eclipsing variables are binary star systems that have orbital planes oriented such that the stars eclipse one another as viewed from Earth. The resulting light curve exhibits two brightness minima of different depths: the primary eclipse (deeper minimum) is from the hotter star passing behind the cooler star, whereas the secondary eclipse is shallower. The study of these systems provides the only direct way to measure the individual masses of the stars. Other measurable parameters include the stars' radii, effective temperatures, and the size, orientation, and inclination of the orbit.

The second extrinsic group is occupied by rotating variables, which show small changes in brightness caused by large dark or bright patches on their surfaces. The period of the varying luminosity is related to the rotational period of the star, coupled with the location and the formation rate of the star spots.

1.3.1 Pulsating Variables

Pulsating variables, hereafter *pulsators*, are stars that experience periodic expansion and contraction of their surface layers. Characteristics of stellar pulsation can be defined by the normal modes of vibration of a star, and by whether the pulsations are radial or non-radial. Radial pulsations involve the entire atmosphere of the star, and conserve spherical symmetry. Non-radial pulsations do not conserve spherical symmetry, and are associated with localized oscillations in the atmosphere.

The normal modes at which stars oscillate are separated into two groups: pressure modes and gravity modes. A *pressure mode* (*p-mode*) oscillation is a propagating acoustic wave where pressure is the restoring force, can be either radial ($\ell = 0$) or non-radial ($\ell \geq 1$), and is associated with substantial pressure variations beneath strategically located ionization zones. A *gravity mode* (*g-mode*) oscillation is a propagating gravity wave where gravity is the restoring force, can only be non-radial, and is associated with convective zones within a radiation-dominant layer.

Main Types of Pulsators

Many classes of pulsators, commonly discovered in clusters, are found in specific locations in the CM-diagram (see Figure 1.6). Main types include Cepheids (δ Cephei and W Virginis), RR Lyraes, Dwarf Cepheids (δ Scuti, SX Phe, and γ Dor), Miras, and β Cephei stars. Although their position in the CM-diagram (luminosity and spectral type) is important in their classification, there are other factors that are necessary to distinctively separate each type, such as the period of pulsation, amplitude of pulsation, population type, and as mentioned earlier the mode of pulsation. Table 1.2 presents a detailed list of the main subclasses mentioned above, along with their defining characteristics.

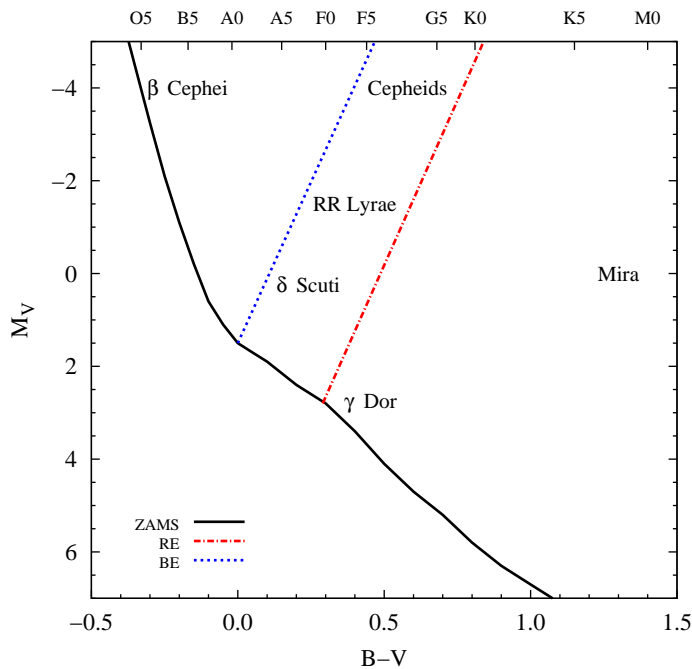


Figure 1.6: CM-diagram that shows the typical locations of the different types of pulsating variables found in clusters. [ZAMS and MK spectral types from data published in Schmidt-Kaler (1982), and IS from data published in Paunzen et al. (2004).]

Main Sequence Variables

δ Scuti stars are pulsators situated on or just above the main sequence within the classical instability strip (see Figure 1.6). The majority of δ Scuti stars pulsate radially ($\ell = 0$) with a large number of low-order ($n = 0$ to 7), low-degree ($\ell \leq 3$), non-radial acoustic modes simultaneously, while some are pure radial pulsators. Multi-periodicity is typical, but not the rule, with a period range from 0.02 to 0.25 days (Breger 2000).

In general, amplitudes are predominantly small, ranging from 0.003 to 0.3 magnitudes in Johnson V . However, there is a subgroup of *High-Amplitude Delta Scuti stars* (HADS), whose pulsation differs from that of the average δ Scuti stars, with V amplitudes ≥ 0.30 magnitudes. The spectral range for δ Scuti stars lies between A0 and F5, which indicates that they are larger and brighter than solar type stars (Breger 2000).

The κ -mechanism is the source that excites and drives p -mode pulsation in δ Scuti stars, as well as other pulsators found in the instability strip. Normally, as a

Table 1.2. Defining characteristics for pulsators

Type	Period (days)	Vis. Amp. (mag)	Spectral Type	Luminosity Class	Population Type	Pulsation Modes ^a
Mira (LPV)	80 – 1000	2.5 – 11.0	Me, Se, Ce	III	I, II	R
β Cephei	0.10 – 0.60	0.01 – 0.3	O8 – B6	I – V	I	R, p
RR Lyrae	0.20 – 1.20	0.2 – 2.0	A – F	III	II	R
γ Dor	0.3 – 3.0	0.001 – 0.1	A7 – F5	IV – V	I	g
Cepheids						
δ Cephei	1 – 35	0.1 – 0.5	F – K	Ib – II	I	R
W Virginis	0.8 – 35	0.3 – 1.2	F – K	Ib – II	II	R
Dwarf Cepheids						
δ Scuti	0.02 – 0.25	0.003 – 0.9	A0 – F5	III – V	I	R, p
SX Phe ^b	0.04 – 0.13	0.3 – 0.9	A0 – F5	IV – V	II	R, p

^a Modes: R = radial, p = non-radial acoustic, g = non-radial gravity.

^b Not shown in Figure 1.6 because they occupy the same region as δ Scuti variables.

References. — General Catalogue of Variable Stars (Samus et al. 2002), Breger (2000), and Warner, Kaye, & Guzik (2003).

region in a star becomes compressed, the opacity (κ) decreases, thus allowing more radiation to pass through. In regions of ionization, however, compression can actually lead to an increase in opacity, which results in a damming-effect to the radiation. The absorption and retention of radiation in the region of high opacity causes an increase in the local temperature and pressure, which pushes out the upper layers of the star and drives pulsation.

A detailed review of δ Scuti stars and their characteristics may be found in Breger (2000), while more information regarding both the physical principles and applications of pulsating stars may be found in Cacciari & Clementini (1990) and Gautschy & Saio (1995, 1996).

1.4 The Problem and Objectives

At this point in our discussion, we have introduced stellar clusters and populations with emphasis on open clusters, identified the four general properties of clusters, discussed the key areas of the HR-diagram as they pertain to clusters, presented the different types of variable stars often found in clusters, and focused on a distinct group of main sequence pulsators, δ Scuti stars.

δ Scuti stars are of particular interest in this study because they represent the transition between the stable behavior of main sequence stars and the unstable nature of pulsators found in the instability strip. Due to the long timescales involved in the stages of stellar evolution, it is not possible to observe the onset of pulsation in any star. However, the fact that $\sim 50\%$ (Breger 2000) of all main sequence stars within the instability strip are δ Scuti stars raises the question of whether the stable stars in the instability strip might be variable with amplitudes below the present detection limit of 0.001 mag (Breger 2000). Hence, the goal of this research was to examine main sequence stars within the classical instability strip for variability.

In terms of variable star searches, open clusters are a natural choice because of their homogeneous properties, their large number of high mass stars, and the large sample size of nearby clusters. As a result, the first stage of this project was to select six clusters based on the following criteria: age, distance from the Sun, angular diameter, and location in the night sky. A range of ages was chosen such that any effects that evolution might have on low-amplitude variability would be evident. The attribute used to represent the age of each cluster and the basis for selection was the highest spectral type member still remaining on the main sequence. Since the project was designed to be performed on the 0.4 m David Derrick Telescope (DDT), only clusters within 1000 pc of the Sun, with angular diameters $\lesssim 23'.0$, and easily observed in the northern hemisphere were chosen.

The primary objective of this research was to apply the *robust median statistic* (hereafter RoMS), developed by Enoch et al. (2003) and expanded by Hintz &

Rose (2005), to the data for the detection of small-amplitude variability. Also, we were curious to find any effects that stellar evolution might have on low-amplitude variability.

1.4.1 Selected Open Clusters

Six open clusters were selected from data published by Becker & Fenkart (1971). However, after an analysis of initial observations, we are led to agree with distance values from the WEBDA database (2006), which claims that three of the clusters are actually ≥ 1200 pc from the Sun, of which NGC 7142 lies at a distance of ~ 1700 pc. The discrepancy in the distance to NGC 7142 proved to be too much for any useful observations on the DDT. Therefore, only the data obtained with the 1.8 m Plaskett Telescope at Dominion Astrophysical Observatory are presented in this thesis.

Table 1.3 lists the most recently published data for the selected clusters as given by Becker & Fenkart (1971), the SIMBAD database (2006), and the WEBDA database (2006). Column (1) gives the cluster name, as given by Becker & Fenkart (1971). Columns (2) and (3) give the right ascension and declination (J2000) of the center of each cluster. Positions are taken from the SIMBAD database (2006). Column (4) gives the distance from the Sun in parsecs, taken from the WEBDA database (2006). Column (5) gives the distance modulus from the Sun in magnitudes, taken from the same source as the distance. Column (6) gives the foreground interstellar reddening, $E(B-V)$, taken from the WEBDA database (2006). Column (7) gives the angular diameter in arc minutes, taken from Becker & Fenkart (1971). These estimates are approximate and biased by field-star contamination. Column (8) gives the logarithm (base 10) of the cluster age in years, taken from the WEBDA database (2006). Column (9) gives the spectral type of the highest cluster member still on the main sequence as determined from the CM-diagram, taken from Becker & Fenkart (1971).

Table 1.3. Open clusters observed in this study

(1)	(2)	(3)	(4)	(5)	(6)	(7)	(8)	(9)
Cluster	RA (h m s)	Dec. ($^{\circ}$ $'$)	Dist. (pc)	Mod. (mag)	$E(B-V)$ (mag)	Dia. ($'$)	Age	Spec. Type
NGC 225	00 43 42	61 47.0	657	9.94	0.274	15	8.114	B8
NGC 559	01 29 22	63 16.8	1258	12.95	0.790	7	7.748	B7
NGC 6811	19 37 10	46 22.5	1215	10.92	0.160	15	8.799	A1
NGC 6940	20 34 24	28 17.0	770	10.10	0.214	26	8.858	A0
NGC 7142	21 45 09	65 46.5	1686	12.36	0.397	11	9.276	F
NGC 7160	21 53 36	62 36.0	789	10.65	0.375	10	7.278	O-B

References. — Becker & Fenkart (1971), SIMBAD database (2006), and WEBDA database (2006).

1.4.2 Current Research

The presentation of this research begins with the photometric observations and the image reduction procedures, which are contained in Chapter 2. Chapter 3 presents the methods of digital aperture photometry, point spread function fitting, differential photometry, and the RoMS as applied to the data. Chapter 4 presents specific results extracted from, and determined by, the methods in Chapter 3. The concluding Chapter includes a discussion of the possible directions in which the research may progress in the future.

Chapter 2

Observations and Reductions

The purpose of this chapter is to familiarize the reader with the equipment used to observe the selected clusters and the basic steps involved in the image reduction process.

2.1 Photometric Observations

All photometric observations of the selected clusters were secured between 2004 July and 2005 October at the Orson Pratt Observatory and the Dominion Astrophysical Observatory (hereafter OPO and DAO, respectively). A total of 5 nights of data were obtained for NGC 225, 3 nights for NGC 559, 5 nights for NGC 6811, 6 nights for NGC 6940, 1 night for NGC 7142, and 5 nights for NGC 7160. Three-color images of the clusters are presented in Figure 2.1.

2.1.1 Orson Pratt Observatory

At OPO, the 0.4 m David Derrick Telescope (DDT) was used with two, telescope focus/CCD combinations:

1. Apogee Ap47p CCD at the Newtonian focus with
 - a 1024×1024 array of $13 \mu\text{m}$ pixels,
 - a plate scale of $1''.32 \text{ pixel}^{-1}$,
 - a $22'.5$ field of view, on a side,
 - a CCD temperature of -24.8° C .

2. SBIG ST-1001 CCD at the Cassegrain focus with
 - a 1024×1024 array of $24 \mu\text{m}$ pixels,
 - a plate scale of $0''.76 \text{ pixel}^{-1}$,

- a 13'0 field of view, on a side,
- a CCD temperature of -28.0° C.

Images were taken using *BVRI* Johnson-Cousins broadband filters, which incorporate filter specifications set by Bessell (1990). Calibration frames – zeros, darks, and flats – were also taken each night for later removal of the system’s instrumental signature during the image reduction process – see § 2.2.

2.1.2 Dominion Astrophysical Observatory

At DAO, the 1.8 m Plaskett Telescope was used with the SITe-5 CCD (1024×1024 array of $24 \mu\text{m}$ pixels) at the Newtonian focus, which yields a plate scale of $0''.54$ pixel $^{-1}$. The field of view (9'0 per side) of this system, much smaller than that on the DDT, was exploited to obtain improved separation of stars in the cores of the clusters. Instead of a particular set of filters, only a Johnson *V* filter was used for the observations at DAO. Calibration frames – zeros and flats – were taken each night, though, due to a CCD temperature of -130° C, darks were not needed.

Table 2.1 lists all photometric observations of the selected open clusters used in this study. Column (1) gives the cluster name, as given in Becker & Fenkart (1971). Column (2) gives the UT date of each night of observations for the cluster listed in the first column. Column (3) gives the site where a particular night of data was taken. The specific telescope focus/CCD configuration for a particular night is denoted with a superscript *a* or *b*. Columns (4)–(7) give the number of observations per filter for the *BVRI* filter system.

2.1.3 Nominal Exposure Lengths

The method of determining the nominal exposure lengths began with a search of the literature for absolute visual magnitudes, M_V , for main sequence stars with spectral types A0 to F5. We chose the data from Schmidt-Kaler (1982), which is

Table 2.1. Photometric observations of open clusters

(1)	(2)	(3)	(4)	(5)	(6)	(7)
Target	Date (UT)	Site	<i>B</i>	<i>V</i>	<i>R</i>	<i>I</i>
NGC 225	02 Nov 2004	OPO ^a	...	100	100	...
	03 Nov 2004	OPO ^a	...	130
	06 Sep 2005	DAO	...	83
	07 Sep 2005	DAO	...	49
	08 Sep 2005	DAO	...	15
NGC 559	14 Dec 2004	OPO ^a	...	50	50	...
	07 Sep 2005	DAO	...	25
	08 Sep 2005	DAO	...	15
NGC 6811	29 Jul 2004	OPO ^a	...	3	3	3
	09 Aug 2004	OPO ^a	...	7	7	7
	06 Sep 2005	DAO	...	125
	08 Sep 2005	DAO	...	25
	15 Oct 2005	OPO ^b	6	6	6	...
NGC 6940	29 Jul 2004	OPO ^a	...	3	3	3
	08 Aug 2004	OPO ^a	...	10	10	10
	09 Aug 2004	OPO ^a	...	12	12	12
	12 Aug 2004	OPO ^a	...	75	75	...
	08 Sep 2005	DAO	...	25
NGC 7142	15 Oct 2005	OPO ^b	6	6	6	...
	07 Sep 2005	DAO	...	41
NGC 7160	09 Aug 2004	OPO ^a	...	10	10	10
	28 Aug 2004	OPO ^a	...	5	5	...
	03 Nov 2004	OPO ^a	...	50	50	...
	08 Sep 2005	DAO	...	15
	15 Oct 2005	OPO ^b	6	6	6	...

^a Apogee Ap47p configuration.

^b SBIG ST-1001 configuration.

widely accepted by the astronomical community. The values obtained were $M_V = 0.6$ (A0), 1.9 (A5), 2.7 (F0), and 3.5 (F5).

The next step was to use the *distance modulus equation* (see Equation 2.1), and the absolute visual magnitude values given above, to calculate a table of apparent visual magnitudes for a list of distances. In Equation 2.1, m_V is the apparent visual magnitude, M_V is the absolute visual magnitude, d is the distance in parsecs to the object, and A_V is the line-of-sight, interstellar absorption or reddening in magnitudes.

$$m_V - M_V = 5 \cdot \log_{10} d - 5 + A_V \quad (2.1)$$

A table of apparent visual magnitude values for a list of distances from the Sun was developed, shown in Table 2.2, under the assumption of no interstellar reddening ($A_V = 0$) between us and the clusters. This assumption allowed us to create a table of approximate values that could be used for any object of known distance. The first column in Table 2.2 gives the list of distances in parsecs. The next four columns give the apparent visual magnitude values, corresponding to the distances in the first column, for the spectral types A0, A5, F0, and F5, respectively. The final column gives the median value in magnitudes of the apparent visual magnitude values in columns 2–5.

The final step was to utilize the relationship between apparent visual magnitude and exposure length developed by Hintz (2004) for the DDT. This relationship allowed us to determine the exposure length needed to obtain high signal-to-noise values for stars of spectral type A0 to F5 at a given distance. Table 2.3 presents the relationship as described by Hintz (2004). Column (1) gives the median value in magnitudes of the apparent visual magnitude as taken from the error versus magnitude plot. Column (2) gives the nominal exposure length in seconds. Columns (3) and (4) give the limits in magnitudes corresponding to the exposure times in Column (2). The values in Column (3) represent the apparent visual magnitudes of the brightest

Table 2.2. Universal table of apparent visual magnitudes

Distance (pc)	Apparent Visual Magnitudes (mag)				Median m_V (mag)
	A0	A5	F0	F5	
200	7.105	8.405	9.205	10.005	8.805
300	7.986	9.286	10.086	10.886	9.686
400	8.610	9.910	10.710	11.510	10.310
500	9.095	10.395	11.195	11.995	10.795
600	9.491	10.791	11.591	12.391	11.191
700	9.825	11.125	11.925	12.725	11.525
800	10.115	11.415	12.215	13.015	11.815
900	10.371	11.671	12.471	13.271	12.071
1000	10.600	11.900	12.700	13.500	12.300
1100	10.807	12.107	12.907	13.707	12.507
1200	10.996	12.296	13.096	13.896	12.696
1300	11.170	12.470	13.270	14.070	12.870
1400	11.331	12.631	13.431	14.231	13.031
1500	11.480	12.780	13.580	14.380	13.180

Note. — These values assume no interstellar reddening, $A_V = 0$.

stars that are just below the saturation limit of the CCD, while Column (4) represents the apparent visual magnitudes of the faintest stars with high errors.

2.2 Image Reductions

The process of standard CCD image reduction utilizes a basic set of images that form the base of the calibration and reduction process. This basic set of images consists of three calibration frames – bias, dark, and flat field – and the data frames of the object(s) of interest. The Image Reduction and Analysis Facility (hereafter IRAF), developed by the National Optical Astronomical Observatories (NOAO), was used for all image reductions.

Table 2.3. Nominal exposure lengths on the 0.4 m David Derrick Telescope

(1)	(2)	(3)	(4)
Median m_V (mag)	Exp. Length (sec)	Sat. Limit (mag)	High Error (mag)
7.0 – 7.9	1.3	5.5	10.5
8.0 – 8.9	3.2	6.5	11.5
9.0 – 9.9	8.0	7.5	12.5
10.0 – 10.9	20.0	8.5	13.5
11.0 – 11.9	50.0	9.5	14.5
12.0 – 12.9	126.0	10.5	15.5
13.0 – 13.9	317.0	11.5	16.5
14.0 – 14.9	796.0	12.5	17.5

References. — Data from Hintz (2004).

2.2.1 Calibration Frames

Bias Frames

Bias frames, often called zeros, allow the user to measure the underlying noise or bias level within each data frame. This bias level is a result of low spatial frequency variations from the on-chip amplifiers, contains the DC offset level or overscan, and should remain constant with time. A bias frame is acquired with the shutter closed and the CCD is simply read out with an exposure time of zero seconds. An average bias image of 10 or more single bias frames was then subtracted from all object and flat field frames taken at DAO.

Dark Frames

Dark frames are a measure of the thermal noise or dark current in a CCD, and provide the user with information about bad or hot pixels. A dark frame is acquired with the shutter closed and for a duration equal to that of the object frames. Observatory class CCD cameras, such as the SITe-5 chip at DAO, are cryogenically

cooled to temperatures where the dark current is essentially zero. As a result, dark exposure CCD frames were not required in the calibration process for images taken at DAO.

Thermoelectrically cooled cameras, such as the AP47p and STE-1001 at OPO, are not cooled to low enough temperatures to ignore the dark current. Thus, an average dark image of 10 or more single dark frames was needed to remove the dark current, and was subtracted from all object and flat field frames taken at OPO. Since dark frames were used, separate bias frames were taken but not needed in the calibration process because the bias level is present in the dark frames as well (see Howell 2000).

Flat Field Frames

Flat field frames, as their name implies, are used to correct or flatten the relative response for each pixel to all wavelengths of incident light. This means that each pixel has a slightly different gain or quantum efficiency value when compared to adjacent pixels. Thus, the ideal flat field image would be spectrally and spatially flat. Although there have been many methods devised to obtain flat field images, all object frames in this study were corrected using twilight flats.

Twilight flats were taken during nautical twilight (about half an hour after sunset) with the CCD illuminated by the night sky with relatively short exposure lengths, so that the CCD was not saturated. Since the pixels have different responses to different colors of light, flat field frames were obtained through each filter that was used for object observations. An average flat field image of 4 or more single flat field frames, for each filter, was obtained, then each object frame was divided by it.

2.2.2 Important CCD Properties

Before image processing can occur, two important CCD properties must be extracted from the raw bias and flat field frames, namely the read noise and the gain. Although they are not used in the image reduction process, they are critical

components to the process of measuring stellar intensities, which converts the analog-to-digital units (ADU) read from the CCD into measured photons.

The first step is to measure the mean pixel value within two raw (or unprocessed) bias frames and two raw flat field images, which we have designated as 1 and 2. It is important to note that the frames must be unprocessed, and that the edge rows, the edge columns, and the overscan regions of the images must not be included when calculating the mean pixel values. The mean values of the bias frames are hereafter represented by \bar{B}_1 and \bar{B}_2 , with corresponding values for the flat field images, \bar{F}_1 and \bar{F}_2 .

The next step is to generate two difference images, $B_1 - B_2$ and $F_1 - F_2$, and measure the standard deviation of these image differences, $\sigma_{B_1-B_2}$ and $\sigma_{F_1-F_2}$. The gain is calculated from the following:

$$\text{Gain} = \frac{(\bar{F}_1 + \bar{F}_2) - (\bar{B}_1 + \bar{B}_2)}{\sigma_{F_1-F_2}^2 - \sigma_{B_1-B_2}^2} \quad (2.2)$$

and the read noise is determined from

$$\text{Read Noise} = \frac{\text{Gain} \cdot \sigma_{B_1-B_2}}{\sqrt{2}} \quad (2.3)$$

The IRAF command, `findgain`, was used to perform all of these steps at once. For more information on `findgain`, type `help findgain` in the IRAF terminal.

It is important to note, however, that no combination of bias and flat field frames (for a particular CCD) will yield identical values for the gain and read noise. Therefore, every possible combination or permutation must be measured in order to obtain values that statistically represent the CCD properties. For instance, if the user has 5 bias frames and 5 flat field frames, then the total number of combinations of two bias frames and two flat field frames is 210. Unfortunately, there is no IRAF command or script available that will automate this process, thus the tedious calculations were

Table 2.4. Summary of CCD properties

Properties	Apogee Ap47p	SBIG STE-1001	DAO SITE-5
Size of Array [X:Y]	1056:1024	1024:1024	1040:1040
Average Temperature [$^{\circ}$ C]	-24.8	-28.0	-130.0
Gain [e^- /ADU]	1.74	1.68	5.0
Read Noise [e^-]	9.67	15.70	11.0
Read Noise [ADU]	5.55	9.33	2.2
Overscan Region [X _i :X _f]	1050:1055	None	1029:1039
[Y _i :Y _f]	2:1023	...	4:1025

done by hand for each of the CCDs. Table 2.4 gives a summary of the properties for the three CCDs, which includes the calculated gain and read noise values.

2.2.3 Image Processing Steps

The steps performed in IRAF during the reduction process are essentially the same for any image obtained with a CCD camera. These steps are outlined as follows:

1. Trim and combine the single bias frames (for cryogenically cooled CCD cameras) or dark frames (for thermoelectrically cooled CCD cameras) into an average bias/dark image with the IRAF command, **zerocombine/darkcombine**.
2. Trim the single flat field frames, subtract the average bias/dark image from each flat field frame, and combine the single flat frames (for each filter) into an average flat field image with the IRAF command, **flatcombine**.
3. Trim the single object frames, subtract the average bias/dark image from each object frame, and divide each object frame by the average flat field image with the IRAF command, **ccdproc**.

For more information on `zerocombine`, `darkcombine`, `flatcombine`, and `ccdproc`, type `help [command]` in the IRAF terminal. In addition, Howell (2000) and Gilliland (1992) are excellent resources for CCD observing and reduction techniques.



Figure 2.1: Three-color image of NGC 225 (*top-left*), NGC 559 (*top-right*), NGC 6811 (*middle-left*), NGC 6940 (*middle-right*), NGC 7142 (*bottom-left*), and NGC 7160 (*bottom-right*). Each image is $23'0$ square to contrast the differing distances and diameters of the clusters [Original frames from DSS, combined by author].

Chapter 3

Photometric Methods

The purpose of this Chapter is to familiarize the reader with the process of obtaining instrumental magnitudes by way of digital aperture photometry and point spread function fitting, the process of correcting instrumental magnitudes for non-photometric seeing conditions with differential photometry, and the process of detecting low-amplitude variability with the RoMS.

3.1 Obtaining Instrumental Magnitudes

Two mainstream methods of photometric analysis were used in this research for the purpose of obtaining instrumental magnitudes, namely digital aperture photometry and point spread function fitting. The first method places a software aperture about the point source profile, as shown in Figure 3.1, and then sums the pixel values within the aperture to provide an estimate of S , the total integrated photometric source signal. The second method fits a two-dimensional function to the point source profile (commonly referred to as a point spread function or PSF), and then uses the integrated value beneath this fitted function as an estimate of S .

3.1.1 Digital Aperture Photometry

Digital aperture photometry is a technique that disregards the shape of the source PSF, and simply collects and sums up the observed counts within a specified aperture centered on the object of interest. The basic application of aperture photometry starts with the selection of a circular software aperture of radius r about the center of the star (see Figure 3.1). The radius r was carefully chosen to be between 2 and 3 times the full-width at half-maximum ($r = 2$ to $3 \cdot \text{FWHM}$), such that it contained ~ 95 to 100% of the flux from the object.

An estimated value for the source intensity, I , was obtained by summing the counts within the area $A = \pi r^2$, and removing the estimated background sky contribution ($n_{pix}\bar{B}$), where n_{pix} is the total number of pixels within A . The average background sky value, \bar{B} , was measured using an inner and outer software annulus, as shown in Figure 3.1, with radii of 15 and 20 pixels, respectively. Instrumental magnitudes were calculated with the IRAF command, `phot`, which uses the following relation

$$m_i = -2.5 \cdot \log_{10} I + C \quad (3.1)$$

where m_i is the instrumental magnitude through some passband filter i , I is the source intensity in that passband per unit time, and C is a constant zero point. The zero point was selected to be 20 mag in order to scale the instrumental magnitudes so that they are comparable to the standard values.

This method works well on fields where the stars of interest are distinctly separated from their neighbors. In clusters, however, many of the stars of interest are situated close to neighboring stars, with some at the point of overlapping (see Figure 3.2). Although the IRAF `fitsky` algorithm, used to compute the background sky contribution, is robust enough to handle overlapping stars, aperture photometry is unable to distinguish counts from multiple sources that lie within an aperture. The result is a systematic error in the instrumental intensities and magnitudes.

3.1.2 Point Spread Function Fitting

PSF fitting is a more sophisticated technique that assumes that the shape of the intensity distribution is the same for every astronomical point source on a given CCD frame (see Figure 3.3), and the size of the distribution is a direct measure of the total brightness of the star. The process of profile fitting begins with the calculation of a standard, average PSF for a number of isolated sources in a frame. Next, the implied PSF is matched and scaled to fit the actual digital data within some radius, r , called the fitting radius (see Figure 3.4). The power of PSF fitting is in its ability

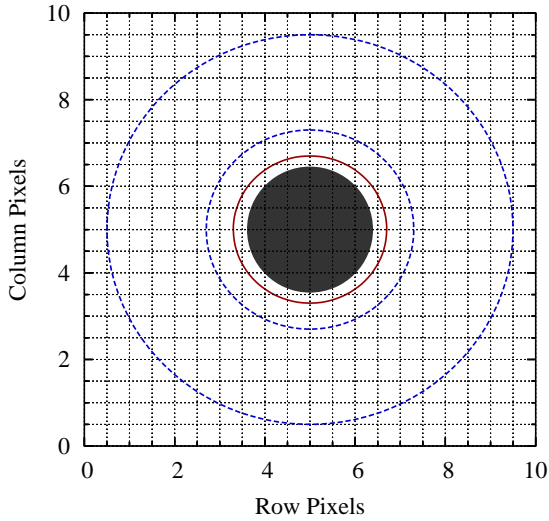


Figure 3.1: Schematic drawing of a stellar source on a CCD pixel grid. The figure shows the location of the star, the aperture (solid line), and the inner and outer sky annuli (dashed circles).

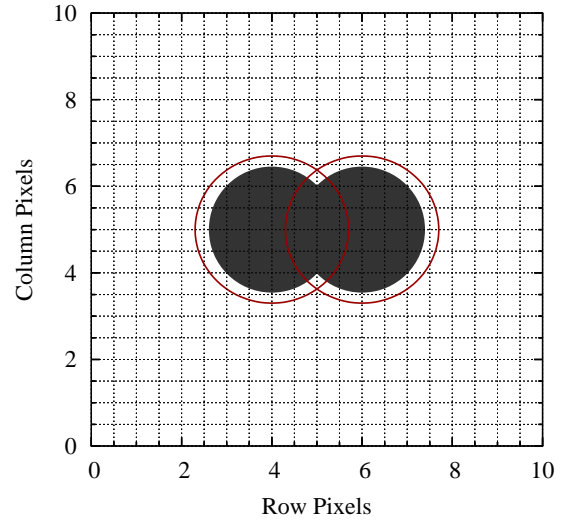


Figure 3.2: Schematic drawing of two overlapping stellar sources on a CCD pixel grid. The figure shows how an aperture (solid line) for one star can include counts from a neighboring star, which results in inaccurate magnitudes.

to produce scientifically valid results for sources whose PSFs overlap (see Figure 3.2), which is accomplished by fitting and removing the intensity distribution from one star before fitting the second star.

DAOPHOT, written by Stetson (1987, 1990, 1991) at DAO, was extensively used throughout this research for the purpose of applying PSF fitting techniques to all stars in the selected clusters. A set of procedures and scripts for DAOPHOT, developed and outlined by Maxwell (2004), were also used during the data reduction process. For more detailed information regarding DAOPHOT and PSF fitting see Maxwell (2004) and Stetson (1987, 1990, 1991).

3.2 Differential Photometry

Differential photometry is a technique that enables the user to remove or minimize the effects of variable seeing, which is to say that the observational data were not obtained under photometric conditions. A particular night is deemed photometric

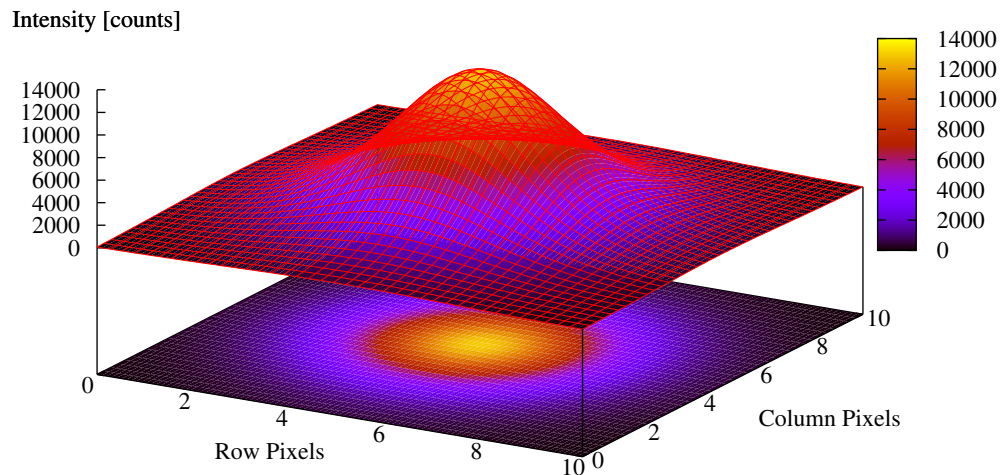


Figure 3.3: A 3-D representation of the 2-D PSF model of the data shown in Figure 3.4. The figure shows how the intensity from a point source object forms an intensity distribution of finite size on a CCD. PSF fitting assumes that the shape of this intensity distribution is the same for all stars on a frame.

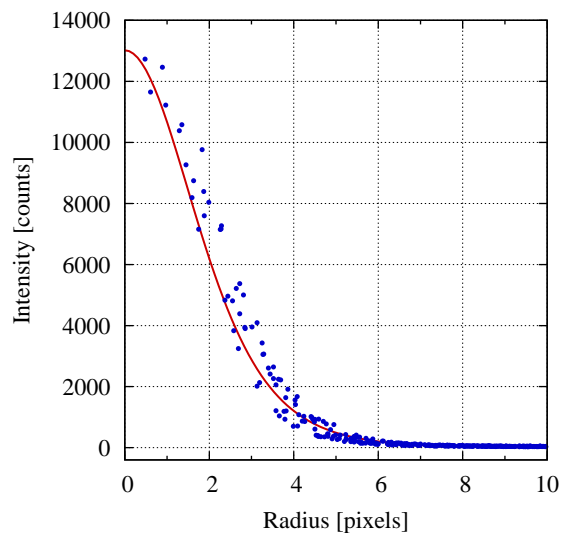


Figure 3.4: A radial plot of a stellar PSF and profile fit. The figure shows how an implied PSF is matched and scaled to fit the actual digital data. The filled circles are the digital data from a star and the line is a fitted Moffat PSF to the data.

when certain criteria important to all-sky photometry are met, such as minimal air and light pollution effects, a low level of humidity or moisture, a dark sky devoid of the Moon and all clouds, and minimal fluctuations within the atmosphere. The method of differential photometry is only valid under the assumption that the effects of variable seeing are uniform across the CCD frame and affect all stars in a similar fashion.

3.2.1 Applying Differential Photometry

The application of differential photometry begins with the selection of an ensemble of comparison stars. It is imperative that the comparison stars are stable or non-variable, and important that the ensemble spans a wide range of magnitudes. The selection process is fairly straightforward for sparse fields of stars where the variable stars of interest are known; however, when dealing with a cluster of several hundred stars, where the variable stars are not known, the selection process is not so apparent.

Once an ensemble has been defined, an average value of the ensemble is calculated for each frame. This average value represents all of the stars in the ensemble, such that any change in the average from frame-to-frame is a result of the atmospheric extinction coupled with the effects of variable seeing. If the seeing conditions were stable throughout the night, then we would expect to find a linear relationship between the magnitude and the *air mass* for a given observation. This relationship represents the atmospheric extinction in magnitudes per air mass, as shown in Figure 3.5.

Figure 3.6 shows how variable seeing conditions and atmospheric extinction can affect the average value of the ensemble over a period of half an hour. The next step is to determine a correction value in magnitudes for each frame, which is done by calculating an average of the average of the ensemble over all frames, and subtracting this average from the average of the ensemble for each frame. The correction value is then applied to all stars in the data set, by corresponding frame, such that all observations for a given star have been corrected for atmospheric extinction and

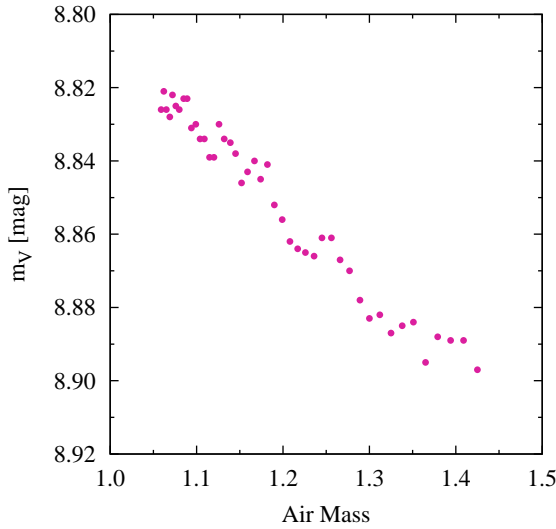


Figure 3.5: An air mass-magnitude diagram of a normal or stable star observed under near-photometric conditions. This figure demonstrates the linear relationship of atmospheric extinction in magnitudes per unit air mass.

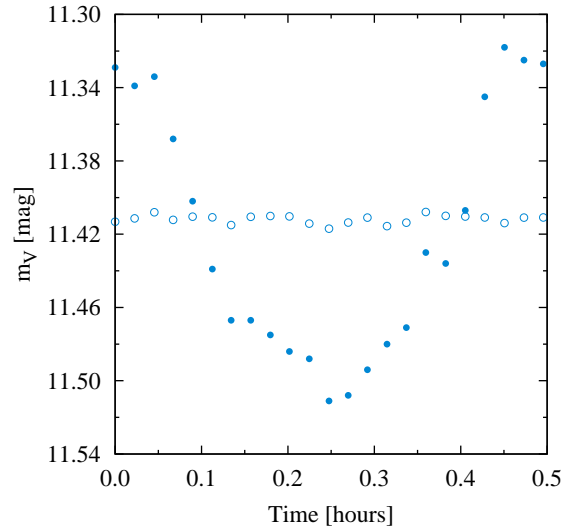


Figure 3.6: A plot of the average value of the ensemble over a period of half an hour. This figure shows how variable seeing and atmospheric extinction can affect the average value of the ensemble (filled circles), and the average value of the ensemble after the correction value has been applied (open circles).

seeing effects. Figure 3.6 also shows the average value of the ensemble after the correction has been applied, which now appears relatively flat.

3.2.2 Differential Photometry Software

A software program, called CLUSTER, was designed and written specifically to aid the user in this selection process, and perform the differential photometry procedures (described above) on a cluster of stars. The program begins by prompting the user for any known variables in the set, which are then removed from the ensemble. Next, CLUSTER uses a user specified *cut value* (the maximum standard error in standard deviations that is allowed to remain in the ensemble) to remove from the ensemble all stars with a standard error greater than or equal to the cut value. The stars that are not specified as variable and have an error less than the cut value now

make up the ensemble. (A user’s guide to CLUSTER along with sample input and output files are given in Appendix A).

Magnitude-Error Diagram

In a *magnitude-error diagram* (ME-diagram), which is a plot of the average magnitude versus the error per observation, the stars form a tight band at low magnitudes that gently widens and slopes up in an exponential fashion at higher magnitudes (see Figure 3.7). This band or sequence is traditionally called an *error curve*, which exhibits the typical characteristics that we would expect; bright stars (at low magnitudes) tend to have a low error due to a high signal-to-noise ratio, while faint stars tend to have larger error on account of a low signal-to-noise ratio.

Normal or stable stars are principally found along this error curve, which suggests that faint stars (located along the curve) should not be removed from the ensemble. Instead, the stars that lie well away from the error curve, as shown in Figure 3.7, should be selected and removed from the ensemble. It is important to note that the region above the error curve in the ME-diagram is where most high-amplitude variables are found.

3.2.3 Outline of Procedures

As a result of this analysis, a set of steps or procedures were developed that would use CLUSTER in its current form, and minimize the probability of including a variable star in the comparison ensemble. The steps are outlined as follows:

1. The instrumental magnitudes from aperture photometry or PSF fitting are loaded into CLUSTER, only previously discovered variables are removed from the ensemble, and a cut value (~ 2.0) is specified such that the ensemble is comprised of all of the stars. CLUSTER outputs a file with the error per observation and average magnitude.

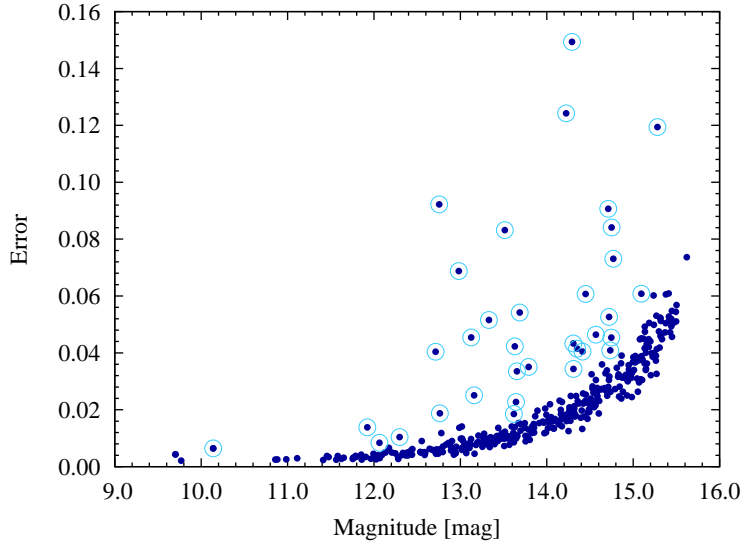


Figure 3.7: A ME-diagram of the cluster NGC 559. This figure shows the formation of the traditional error curve. Stable stars are principally found along the bottom of this curve, while most high-amplitude variables are found in the region well above the error curve. Stars that were selected for further examination and removed from the comparison ensemble are circled.

2. A ME-diagram is constructed from the output of CLUSTER, and all stars that lie well above the error curve are identified and recorded (see Figure 3.7).
3. The original instrumental magnitudes are reloaded into CLUSTER, the recorded stars from step 2 are removed from the ensemble, and a cut value (again ~ 2.0) is specified such that the new ensemble is comprised of all remaining stars. CLUSTER outputs a file with the average magnitude and more precise values of the error.
4. Steps 2 and 3 may be repeated several more times to see if any other stars move away from the error curve.

The result is a list of stars that should be examined more closely for high-amplitude variability.

3.3 Robust Median Statistic

The RoMS is a statistical method that was originally developed by Enoch et al. (2003) for the purpose of detecting small-amplitude variability among L and T-type dwarfs. This method was expanded later by Hintz & Rose (2005) for use on stellar clusters, applied to the field NGC 6682/85, and found to be very effective. As a result, the primary objective of this research was to apply the RoMS in a similar fashion as Hintz & Rose (2005) but to multiple clusters of differing ages.

3.3.1 Defining the RoMS

The RoMS value, $\tilde{\eta}$, is defined by Enoch et al. (2003) as

$$\tilde{\eta} = \eta/d \tag{3.2}$$

where d is the number of degrees of freedom or $(N-1)$, N is the number of observations, and η is represented by the following relation,

$$\eta = \sum_{i=1}^N \left| \frac{m_i - \bar{m}}{\sigma_i} \right| \tag{3.3}$$

Equation 3.3 consists of the following terms: m_i is the magnitude of the i^{th} observation, \bar{m} is the *median* value (not the average) of N observations, and σ_i is the minimum error value corresponding to magnitude, m_i , from the bottom of the error curve in the ME-diagram (see Figure 3.7). How to define an analytical function to represent the bottom of the error curve is discussed in §§ 3.3.2.

Interpreting the RoMS

Enoch et al. (2003) have established that stars with a RoMS value of $\tilde{\eta} \geq 1.0$ have a high probability of being variable, while a value of $\tilde{\eta} < 1.0$ suggests that the star is not likely to be variable. Moreover, Enoch et al. (2003) quantified these values

by running Monte Carlo simulations. Hintz & Rose (2005) add that stars with a RoMS value between 0.8 and 1.0 have a 50% probability of being variable.

3.3.2 Defining the Analytical Function

Before the RoMS could be applied to the observational data, an analytical function, to represent the bottom of the error curve, was needed in order to efficiently determine the minimum error, σ_i , for each observation of each star in the cluster. The best method discovered to date begins with taking the natural logarithm of the errors and plotting them versus the magnitude; note that this is the same thing as plotting the ME-diagram on a semi-log scale. Figure 3.8 is an example of a typical semi-log ME-diagram.

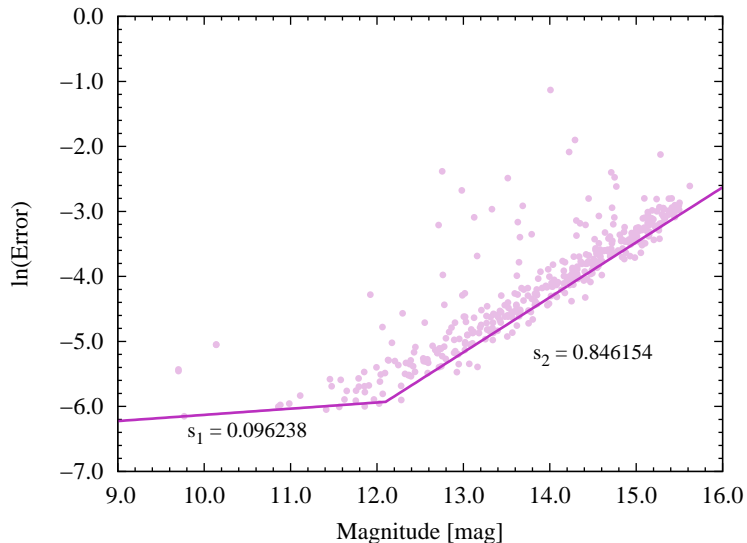


Figure 3.8: A semi-log ME-diagram of the cluster NGC 559. This figure shows how two lines with different slopes were used to represent the bottom of the error curve. The values of each slope are given.

From this figure, we ascertained that two distinct slopes are present: the first is almost horizontal and stretches from 9.0 to 12.1 magnitudes, while the second follows

a greater angle and spans 12.1 to 16.0 magnitudes. It is important to note that these ranges are only valid for this cluster and for this particular set of data. Furthermore, a semi-log ME-diagram should be created and the ranges should be determined for each cluster and each night of data. The first slope, s_1 , was estimated by drawing a line that intersected at least one data point and approximated the bottom of the error curve from 9.0 to ~ 12 magnitudes, while the second slope, s_2 was determined in the same manner but from ~ 12 to 16.0 magnitudes. The values of each slope are given in Figure 3.8.

As a result of the large difference between the two slopes, a single exponential function of the form

$$\sigma_i(x) = a_0 \cdot e^{a_1 \cdot x} \quad (3.4)$$

was found to be insufficient in approximating the bottom of the entire error curve, whereas a piecewise continuous function of the form

$$\sigma_i(x) = \begin{cases} b_0 \cdot e^{b_1 \cdot x} & x_0 \leq x < x_1 \\ c_0 \cdot e^{c_1 \cdot x} & x_1 \leq x \leq x_2 \end{cases} \quad (3.5)$$

was found to approximate the bottom of the entire error curve very well (see Figure 3.9). In Equation 3.5, the exponential coefficients, b_1 and c_1 , are the slopes, s_1 and s_2 , respectively. The coefficients, b_0 and c_0 , are found using a data point that lies along the first line and the value of the first function at the point where line 1 and line 2 intersect; this ensures that the piecewise function is continuous. x_0 , x_1 , and x_2 are the boundary values determined from the lines drawn on the semi-log ME-diagram, as shown in Figure 3.8.

The resulting piecewise continuous function is

$$\sigma_i(x) = \begin{cases} 8.4 \times 10^{-4} \cdot e^{0.096 \cdot x} & 9.0 \leq x < 12.1 \\ 9.5 \times 10^{-8} \cdot e^{0.846 \cdot x} & 12.1 \leq x \leq 16.0 \end{cases} \quad (3.6)$$

and is drawn in Figure 3.9. It is important to note that all data points that fall below this line are treated as though they lie on the line with the minimal error value.

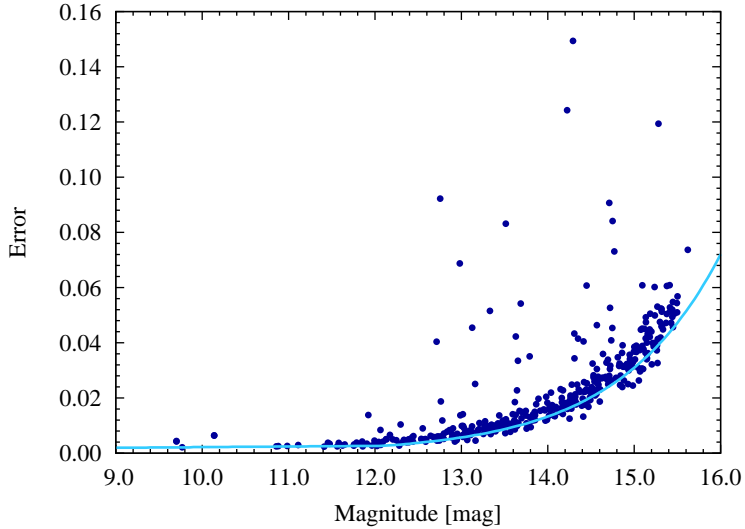


Figure 3.9: ME-diagram of the cluster NGC 559 with the RoMS analytical function. This figure shows how the analytical function approximates the bottom of the error curve. All data points that lie below the line are treated as though they lie on the line with the minimal error value.

3.3.3 RoMS Software

A software program written in C, called ROMS, was developed specifically to accelerate the process of applying the RoMS technique to cluster data. The program uses the coefficients defined by the piecewise continuous analytical function (see Eq. 3.5), the boundary value or intercept between the two parts of the function, and the magnitude output file from CLUSTER to calculate the RoMS value for each star. A user’s guide to ROMS and sample output file are given in Appendix B.

3.3.4 Outline of Procedures

A summary or outline of the procedures involved in defining the analytical function and applying the RoMS is given below:

1. Plot the ME-diagram on a semi-log scale (natural logarithm of the error values) as shown in Figure 3.8.
2. Draw and calculate the slope of a line that approximates the flatter portion of the semi-log ME-diagram, which is generally located between 9.0 and 12.0 magnitudes. The line should intersect at least one data point.
3. Draw and calculate the slope of a second line that approximates the steeper portion of the semi-log ME-diagram, which typically resides between 12.0 and 16.0 magnitudes. The second line should intersect the first line at one point and at least one data point along the steeper-sloped data.
4. Determine the boundary values of the two lines along the x -axis (i.e. [9.0,12.1) and [12.1,16.0]) from the limits of the plot and the point of intersection of the two lines.
5. Calculate the coefficient, b_0 , using a data point that lies along the first line. The first part of the analytical function should now be defined.
6. Calculate the second coefficient, c_0 , using the value of the first part of the piecewise function at the point of intersection of the two lines. The piecewise continuous function for σ_i should now be defined.
7. Determine the RoMS value, $\tilde{\eta}$, for each star using Equations 3.2, 3.3, and 3.5. This is accomplished rapidly and efficiently with the program, ROMS (see Appendix B).

Chapter 4

Results and Analysis

RoMS values were determined for all stars in the fields of NGC 225, NGC 559, NGC 6811, NGC 6940, NGC 7142, and NGC 7160. Figure 4.1 presents the RoMS values for the cluster NGC 225 in histogram form. The stars were separated into a variable group and a non-variable group, based upon the inspection of time-series data of all stars with a RoMS value above 0.9. The variable group, denoted by the dark-color bars, includes stars that exhibited periodic variability as well as stars that displayed other forms of variability. The non-variable group, denoted by the light-color bars, is comprised of stars with RoMS values below 0.9 or that did not exhibit any form of variability. Figures 4.2 – 4.6 present the RoMS values in histogram form for the clusters NGC 559, NGC 6811, NGC 6940, NGC 7142, and NGC 7160, respectively, and follow the guidelines given above.

4.1 Statistical Distributions

From Figures 4.1 – 4.6, we see that the RoMS values of the non-variable stars form essentially gaussian-shaped, statistical distributions which appear to be centered about a RoMS value of 0.9. Because the center values of the distributions are similar for all clusters, we therefore conclude that the location of the distribution of non-variable stars is not dependent upon the age of the cluster. These results are not surprising since they match those of Hintz & Rose (2005) and Woodland (2006).

The shape and center of the distributions of potential variable stars, as portrayed in Figures 4.1 – 4.6, are not as well-defined as those of the non-variable stars. In Figures 4.1 and 4.6, we find that the shape of the variable distributions are reasonably defined, whereas in Figures 4.2 – 4.5 the distributions appear somewhat scattered and random. This result is attributed to the fact that the clusters NGC 225

and NGC 7160 have a much larger ratio of potential variables to non-variable stars ($\approx 20\%$), while the histograms of the other clusters are affected more by their large number of non-variables.

If we assume that the shape and location of the statistical distribution of variable stars is the same for all clusters and independent of age, then all of the potential variable stars may be collected and treated as one sample. Figure 4.7 is a histogram of the RoMS values for all potential variables from all of the clusters, and displays an unusual distribution shape. The cause of this unusual shape is uncertain. Perhaps the shape and location of the variable distribution for each cluster is unique and/or dependent upon some unknown factor, such as age. In any case, further investigation of this subject is warranted.

Hintz & Rose (2005) found that the percentage of new variables to total stars was 50% for RoMS values between 0.8 and 1.0. As can be seen in Figures 4.1 – 4.6, only a handful of potential variable candidates were found in this region, which is nowhere near the 50% that was expected. As a result of these findings, the percentage of potential variables to total stars, with RoMS values between 0.8 and 1.0, appears to be unique to each cluster of stars and should not be assumed as a universal relation.

4.2 Potential Variable Stars

Twenty-two new variables and eighty-seven suspected variable stars were discovered with the RoMS method, as explained in § 3.3. Figure 4.8 shows an ME-diagram of NGC 6940 (which had the most new variables found within its field) with the new variables, suspects, and non-variables represented by filled circles, filled diamonds, and open circles, respectively. An interesting feature is that four of the new variables are so close to the error curve that they were not detected using the traditional error curve approach, which demonstrates the powerful capabilities of the RoMS method.

Tables 4.1 – 4.6 present the RoMS results for all of the potential variable stars. Column (1) gives the star name (as a number) assigned in this study, while Column (2)

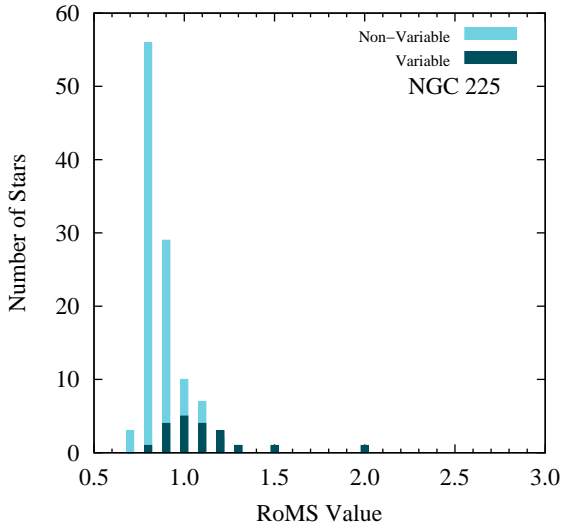


Figure 4.1: Histogram of the RoMS values for all stars in the field of NGC 225. This figure shows the skewed gaussian distribution of the non-variable stars, while the sample of variables is too small to determine a distribution shape.

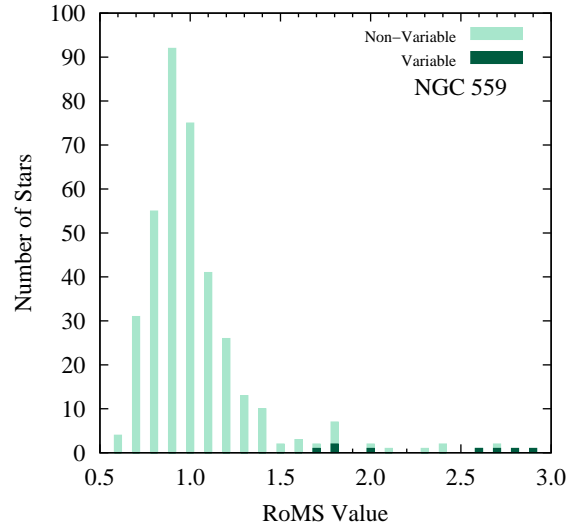


Figure 4.2: Histogram of the RoMS values for all stars in the field of NGC 559. This figure displays the gaussian distribution for the large sample of non-variables in NGC 559, whereas the variables appear under-sampled.

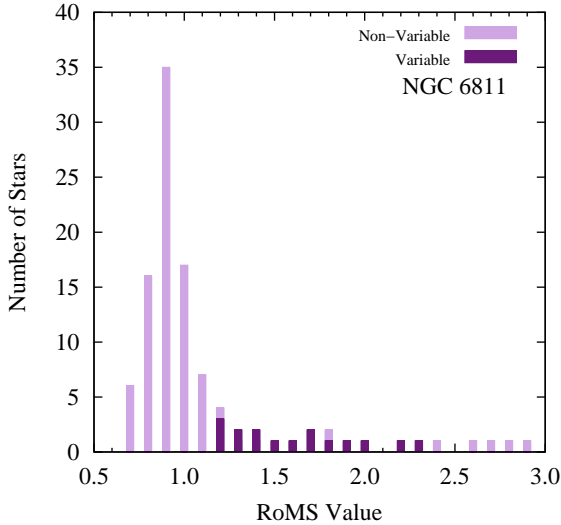


Figure 4.3: Histogram of the RoMS values for all stars in the field of NGC 6811. This figure exhibits a larger sample of variables than the other clusters, but the shape of the distribution is difficult to discern.

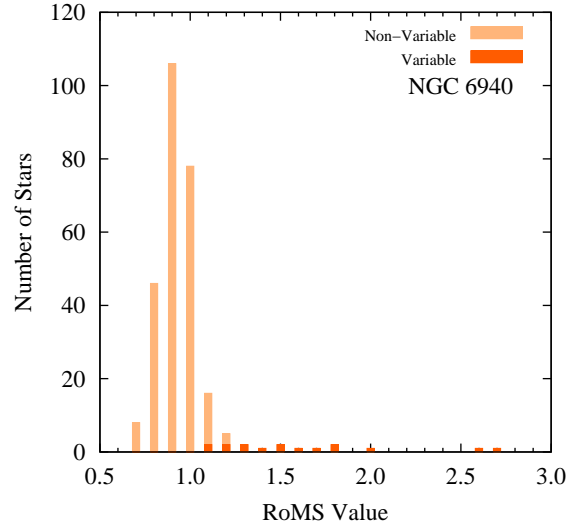


Figure 4.4: Histogram of the RoMS values for all stars in the field of NGC 6940. This figure presents the relative distributions for the non-variable stars and the variables.

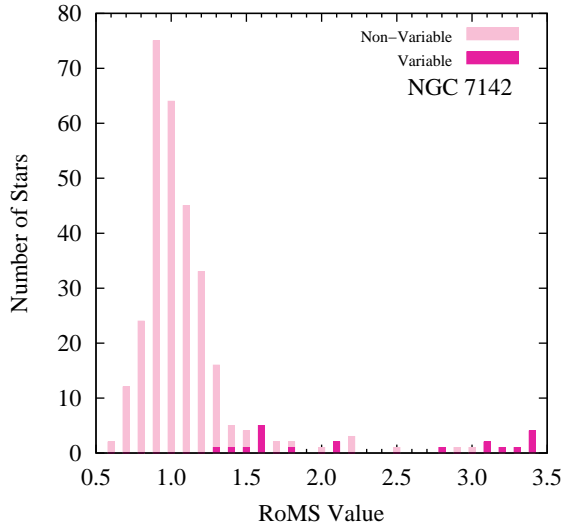


Figure 4.5: Histogram of the RoMS values for all stars in the field of NGC 7142. This figure shows how the RoMS values of the variables appear almost bimodal, while the non-variables form a typical gaussian distribution near $\tilde{\eta} = 0.9$.

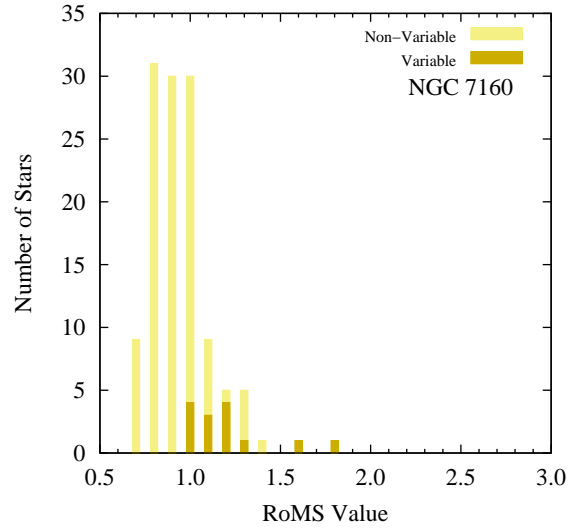


Figure 4.6: Histogram of the RoMS values for all stars in the field of NGC 7160. This figure is deceptive in that the ratio of variables to non-variables is larger than the other clusters.

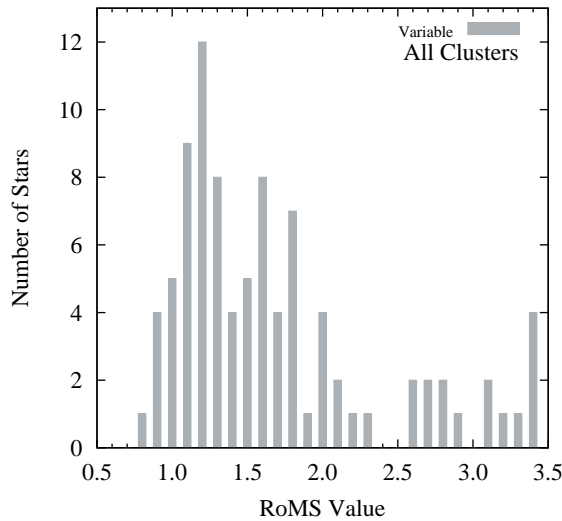


Figure 4.7: Histogram of the RoMS values for all variables found in the fields of the selected clusters. This figure portrays the unusual distribution shape of the variables.

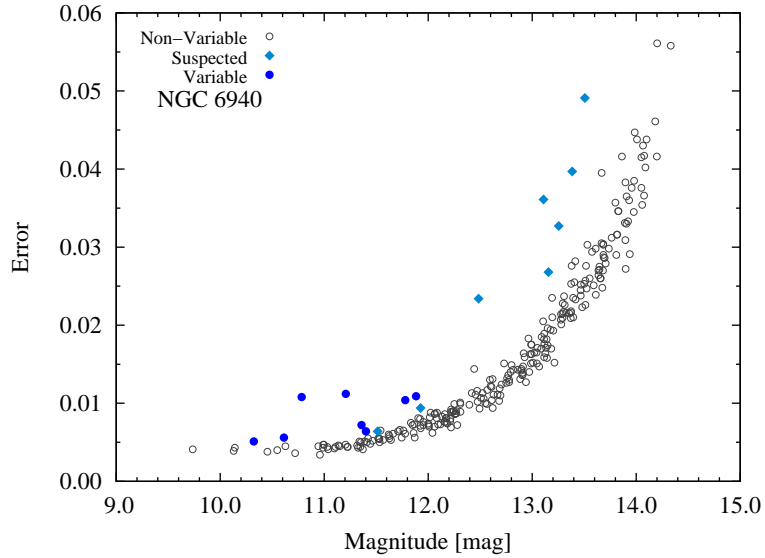


Figure 4.8: An ME-diagram of the cluster NGC 6940 for observations obtained on August 12, 2004 at OPO. This figure shows the location of the new and suspected variables in the ME-diagram, which are represented by filled circles and filled diamonds, respectively. Four of the eight new variables are found very close to the error curve, and would not have been found using the traditional error curve approach.

gives the published star number from the literature. Column (3) gives the RoMS value and Column (4) gives the average, instrumental magnitude in V . Column (5) is used to differentiate between stars that exhibit periodic variability and stars that display another form of variability. The last Column contains comments about the time-series data and the type of variability exhibited by the star. Figures 4.9 – 4.14 present finder charts of the potential variable stars within the field of each cluster.

Table 4.1. Potential variable stars in NGC 225

(1)	(2)	(3)	(4)	(5)	(6)
Star	Pub.	RoMS	\bar{V}	Variable?	Comments
6	...	0.967	12.4151	Susp.	No distinct pattern to variability is evident
16	...	0.987	11.4216	Susp.	Long period variable?
19	1	1.238	8.9242	Susp.	No distinct pattern to variability is evident
22	...	0.974	14.1375	Susp.	No distinct pattern to variability is evident
34	...	1.108	11.1416	Susp.	Multi-periodic pattern
35	23	1.482	12.8222	Yes	Single maximum in 4 hours
40	22	0.774	12.3804	Susp.	No distinct pattern to variability is evident
42	...	1.339	10.5790	Yes	Long period variable?
47	28	1.260	13.3781	Susp.	No distinct pattern to variability is evident
53	18	0.889	11.7636	Susp.	No distinct pattern to variability is evident
57	...	1.143	10.4842	Susp.	No distinct pattern to variability is evident
61	17	1.082	11.3297	Susp.	No distinct pattern to variability is evident
66	...	2.022	10.3966	Yes	Small amplitude of ≈ 0.005 mags
68	8	1.249	9.8173	Yes	Long period variable?
74	1285	0.909	13.7617	Susp.	No distinct pattern to variability is evident
86	...	1.052	13.8851	Susp.	No distinct pattern to variability is evident
87	4054	1.007	11.3467	Susp.	No distinct pattern to variability is evident
105	1221	0.911	12.7509	Susp.	No distinct pattern to variability is evident
107	...	0.857	13.6089	Susp.	No distinct pattern to variability is evident
109	1219	0.955	13.7308	Susp.	No distinct pattern to variability is evident
111	2	1.247	9.3352	Susp.	No distinct pattern to variability is evident

References. — Published star numbers < 1000 from Hoag et al. (1961) and > 1000 from Ponomareva (1983).

Table 4.2. Potential variable stars in NGC 559

(1)	(2)	(3)	(4)	(5)	(6)
Star	Pub.	RoMS	\bar{V}	Variable?	Comments
38	...	1.758	14.7200	Susp.	Slight increase in brightness
71	...	6.167	14.2236	Susp.	No distinct pattern to variability is evident
86	64	3.316	13.1592	Susp.	No distinct pattern to variability is evident
95	...	1.846	14.3496	Susp.	No distinct pattern to variability is evident
102	...	3.138	12.7626	Susp.	No distinct pattern to variability is evident
103	...	2.664	12.2960	Susp.	No distinct pattern to variability is evident
155	...	2.578	13.6550	Yes	Multi-periodic pattern
171	...	2.811	14.7496	Yes	Multi-periodic pattern
185	...	7.418	14.2914	Susp.	No distinct pattern to variability is evident
226	...	24.366	14.0080	Susp.	No distinct pattern to variability is evident
237	...	4.269	11.9232	Susp.	No distinct pattern to variability is evident
256	56	5.248	13.3300	Susp.	No distinct pattern to variability is evident
261	...	2.021	14.3078	Susp.	No distinct pattern to variability is evident
294	52	7.322	12.7130	Susp.	No distinct pattern to variability is evident
297	...	5.454	13.1244	Susp.	No distinct pattern to variability is evident
298	...	7.487	12.9818	Susp.	No distinct pattern to variability is evident
334	...	2.867	14.4489	Yes	Increase in brightness of ≈ 0.15 mags
353	...	1.741	13.6191	Yes	Multi-periodic pattern, brightness decrease

References. — Published star numbers from Lindoff (1969).

Table 4.3. Potential variable stars in NGC 6811

(1)	(2)	(3)	(4)	(5)	(6)
Star	Pub.	RoMS	\bar{V}	Variable?	Comments
8	39	1.395	9.5060	Yes	Single maximum, amplitude ≈ 0.02 mags
30	32	1.715	9.2877	Yes	Brightness increase of 0.03 mags
35	18	1.207	10.0713	Yes	Very multi-periodic
41	70	1.916	8.8666	Yes	Single maximum, multi-periodic?
46	124	1.217	11.3319	Susp.	Decrease in magnitude, no increase evident
48	62	1.419	10.7240	Susp.	Long period variable?
50	58	1.274	11.8380	Susp.	Long period variable?
57	56	1.276	10.0716	Susp.	Multi-periodic, decrease in magnitude
61	113	2.015	9.4540	Susp.	Drastic jump or increase in magnitude
62	54	2.260	10.2431	Yes	Multi-periodic, eclipse?
63	53	2.159	10.5582	Susp.	Decrease in magnitude, no increase evident
65	9	1.159	9.9747	Susp.	Multi-periodic pattern
66	51	1.574	11.2876	Susp.	Multi-periodic pattern
82	4	1.684	10.6556	Susp.	Multi-periodic pattern
93	...	1.830	13.9357	Susp.	No distinct pattern to variability is evident
102	...	1.790	13.2620	Susp.	Slight increase in brightness
113	...	1.478	14.3781	Susp.	No distinct pattern to variability is evident

References. — Published star numbers from Lindoff (1972).

Table 4.4. Potential variable stars in NGC 6940

(1)	(2)	(3)	(4)	(5)	(6)
Star	Pub.	RoMS	\bar{V}	Variable?	Comments
10	...	1.123	10.3235	Yes	Period \approx 2 hrs, amplitude \approx 0.02 mags
32	...	1.527	11.8831	Yes	Multi-periodic pattern
67	...	1.954	12.4843	Susp.	No distinct pattern to variability is evident
91	...	1.954	11.4011	Yes	Eclipser?
99	...	1.512	11.3588	Yes	Amplitude \approx 0.03 mags
134	...	1.387	13.2550	Susp.	No distinct pattern to variability is evident
162	...	1.182	11.9265	Susp.	Multi-periodic?
173	...	1.219	11.5136	Susp.	No distinct pattern to variability is evident
184	...	1.595	13.3852	Susp.	No distinct pattern to variability is evident
192	...	2.745	11.2079	Yes	Period \approx 1.5 hrs, amplitude \approx 0.03 mags
196	...	1.829	13.1087	Susp.	No distinct pattern to variability is evident
198	...	1.299	10.6124	Yes	Period \approx 1.2 hrs, amplitude \approx 0.02 mags
214	...	2.610	10.7831	Yes	Period $>$ 3.5 hrs, amplitude \approx 0.03 mags
243	...	1.808	13.5060	Susp.	No distinct pattern to variability is evident
258	...	1.109	13.1570	Susp.	No distinct pattern to variability is evident
262	...	1.674	11.7800	Yes	Period \approx 1.2 hrs, amplitude \approx 0.03 mags

Table 4.5. Potential variable stars in NGC 7142

(1)	(2)	(3)	(4)	(5)	(6)
Star	Pub.	RoMS	\bar{V}	Variable?	Comments
1	190	3.148	10.7646	Susp.	Decrease in brightness, no increase evident
11	171	1.469	11.7451	Susp.	No distinct pattern to variability is evident
28	1413	1.619	15.0538	Susp.	Multi-periodic pattern
34	235	3.075	11.9581	Yes	Period > 2 hrs, amplitude ≈ 0.02 mags
56	135	1.597	12.3379	Susp.	Eclipser?
122	240	1.301	11.3925	Susp.	No distinct pattern to variability is evident
137	59	1.447	14.1239	Susp.	Multi-periodic pattern
141	193	3.412	11.6169	Susp.	No distinct pattern to variability is evident
170	...	1.616	13.5725	Susp.	No distinct pattern to variability is evident
173	...	1.616	13.5725	Susp.	No distinct pattern to variability is evident
215	1265	4.505	14.0182	Susp.	No distinct pattern to variability is evident
228	198	3.250	12.9918	Susp.	No distinct pattern to variability is evident
242	1057	3.373	13.7916	Susp.	No distinct pattern to variability is evident
244	102	2.763	12.5275	Susp.	Increase in brightness
250	103	3.222	13.3376	Susp.	No distinct pattern to variability is evident
279	148	2.052	13.3661	Susp.	Increase in brightness
286	149	1.844	12.1079	Susp.	Multi-periodic, eclipser?
297	219	1.557	13.5238	Susp.	Decrease in brightness
300	1268	3.426	14.7651	Susp.	No distinct pattern to variability is evident
320	...	2.121	12.1480	Susp.	Decrease in brightness

References. — Published star numbers from van den Bergh & Heeringa (1970).

Table 4.6. Potential variable stars in NGC 7160

(1)	(2)	(3)	(4)	(5)	(6)
Star	Pub.	RoMS	\bar{V}	Variable?	Comments
13	...	1.097	11.1980	Susp.	Decrease in brightness
28	15	0.839	10.4922	Susp.	Multi-periodic pattern
37	...	1.579	12.9688	Susp.	No distinct pattern to variability is evident
44	47	5.972	12.0031	Susp.	No distinct pattern to variability is evident
61	...	1.180	13.5696	Susp.	No distinct pattern to variability is evident
67	55	1.774	11.9167	Susp.	No distinct pattern to variability is evident
71	4	1.156	8.5723	Susp.	Decrease in brightness
74	10	0.825	10.7996	Susp.	Multi-periodic pattern
79	...	1.320	13.6190	Susp.	No distinct pattern to variability is evident
83	...	1.035	12.1599	Susp.	No distinct pattern to variability is evident
95	...	1.039	12.8994	Susp.	No distinct pattern to variability is evident
99	...	1.084	13.7369	Susp.	No distinct pattern to variability is evident
102	...	1.048	13.1167	Susp.	No distinct pattern to variability is evident
117	...	1.146	12.8818	Susp.	No distinct pattern to variability is evident
120	...	1.044	13.0101	Susp.	No distinct pattern to variability is evident
125	...	1.163	13.3991	Susp.	No distinct pattern to variability is evident
134	...	1.190	12.6382	Susp.	No distinct pattern to variability is evident

References. — Published star numbers from Hoag et al. (1961).

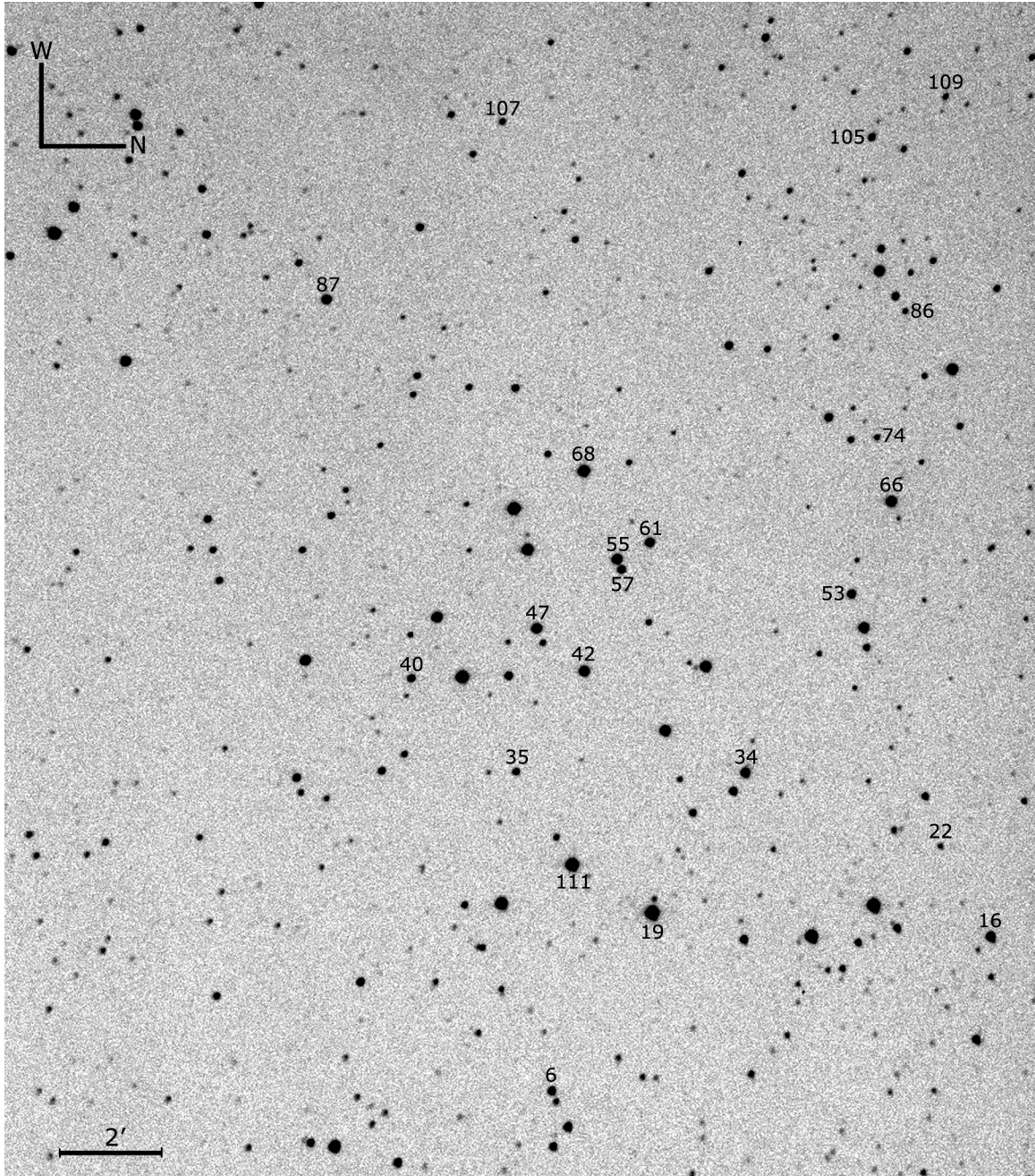


Figure 4.9: A finder chart for potential variables found in the field of NGC 225. This image was taken on November 02, 2004 at OPO with the Apogee Ap47p CCD camera.

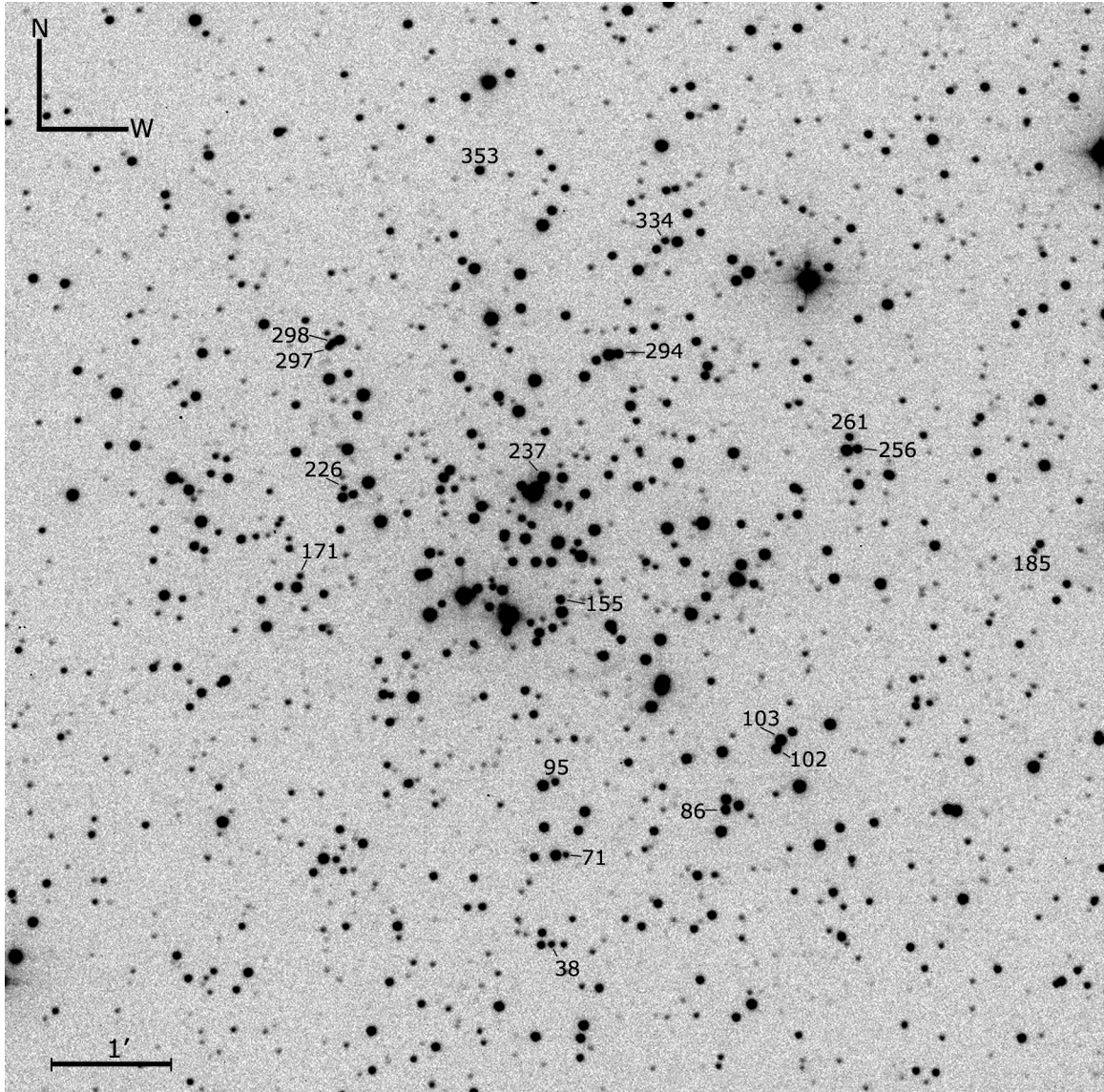


Figure 4.10: A finder chart for potential variables found in the field of NGC 559. This image was taken on September 07, 2004 at DAO with the SITE-5 CCD camera.

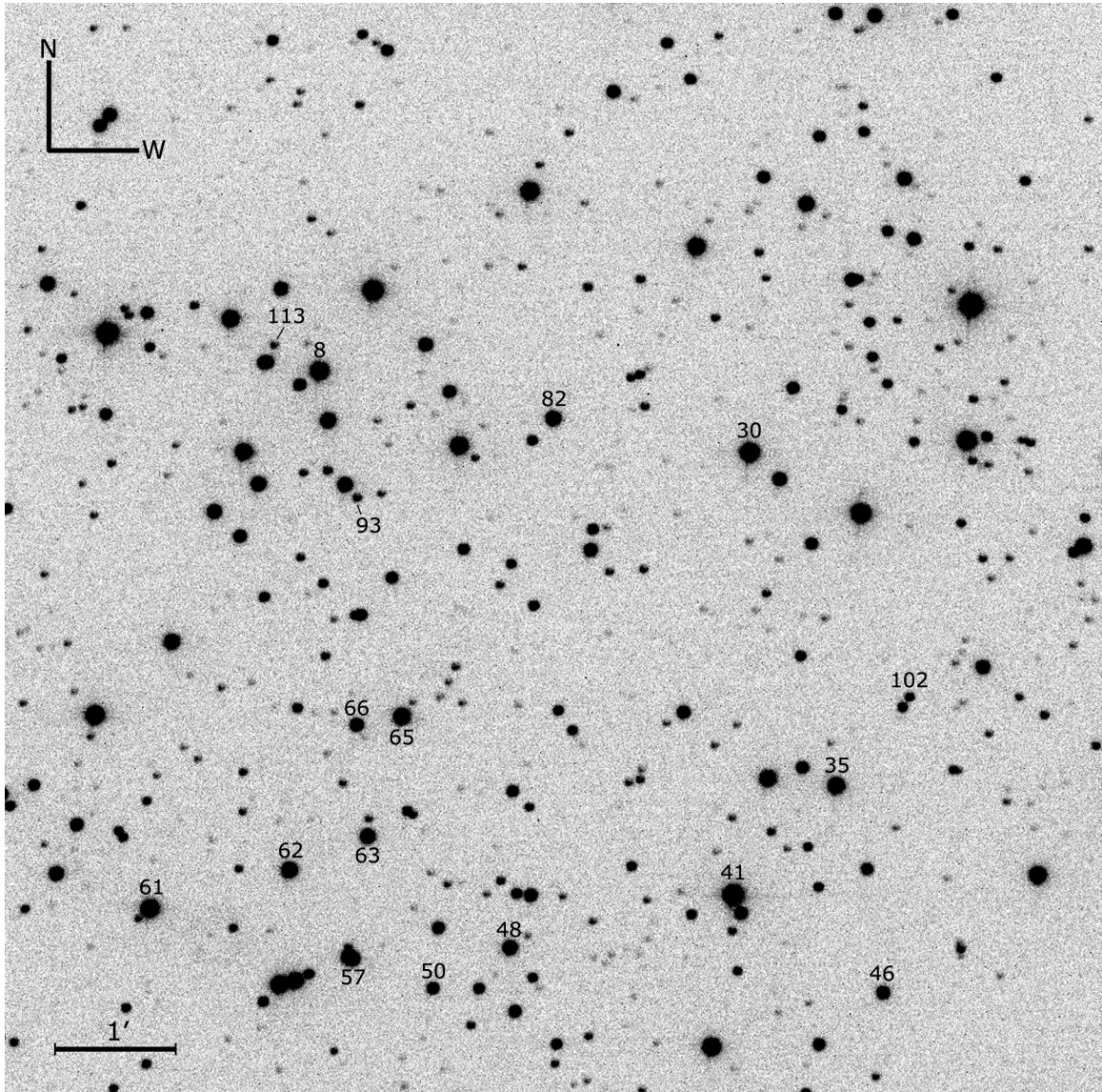


Figure 4.11: A finder chart for potential variables found in the field of NGC 6811. This image was taken on September 06, 2004 at DAO with the SITE-5 CCD camera.

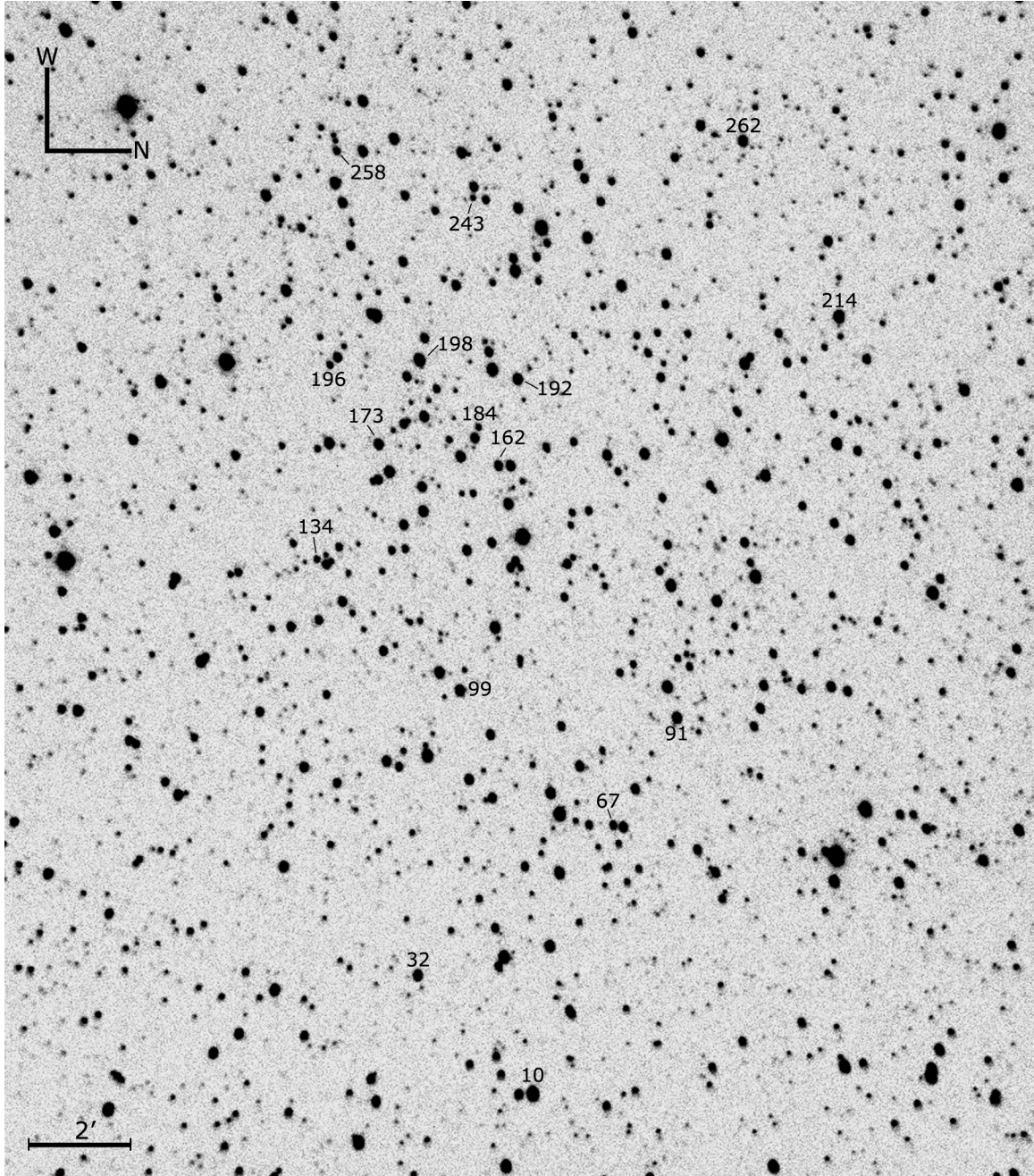


Figure 4.12: A finder chart for potential variables found in the field of NGC 6940. This image was taken on August 12, 2004 at OPO with the Apogee Ap47p CCD camera.

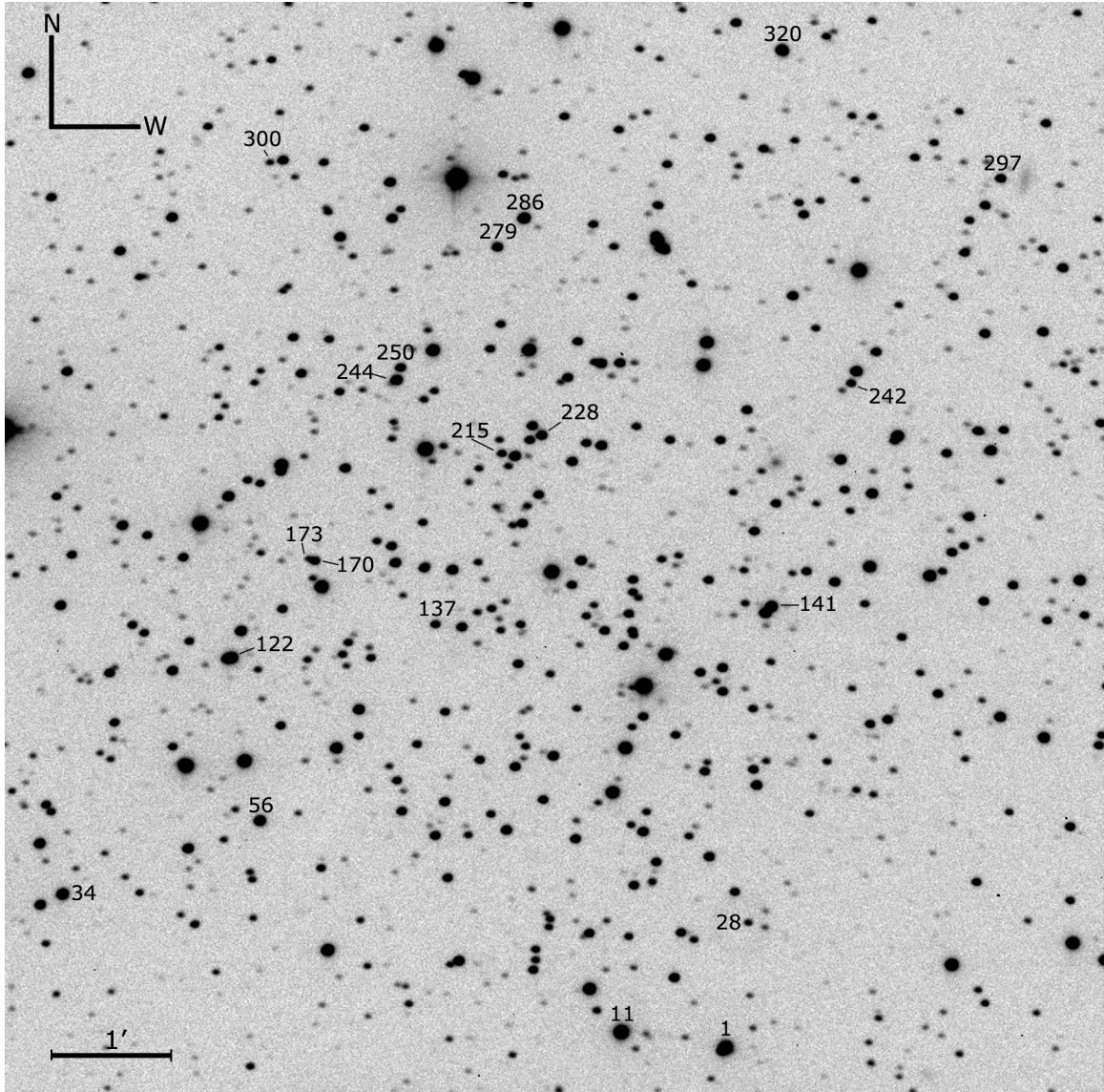


Figure 4.13: A finder chart for potential variables found in the field of NGC 7142. This image was taken on September 07, 2004 at DAO with the SITE-5 CCD camera.

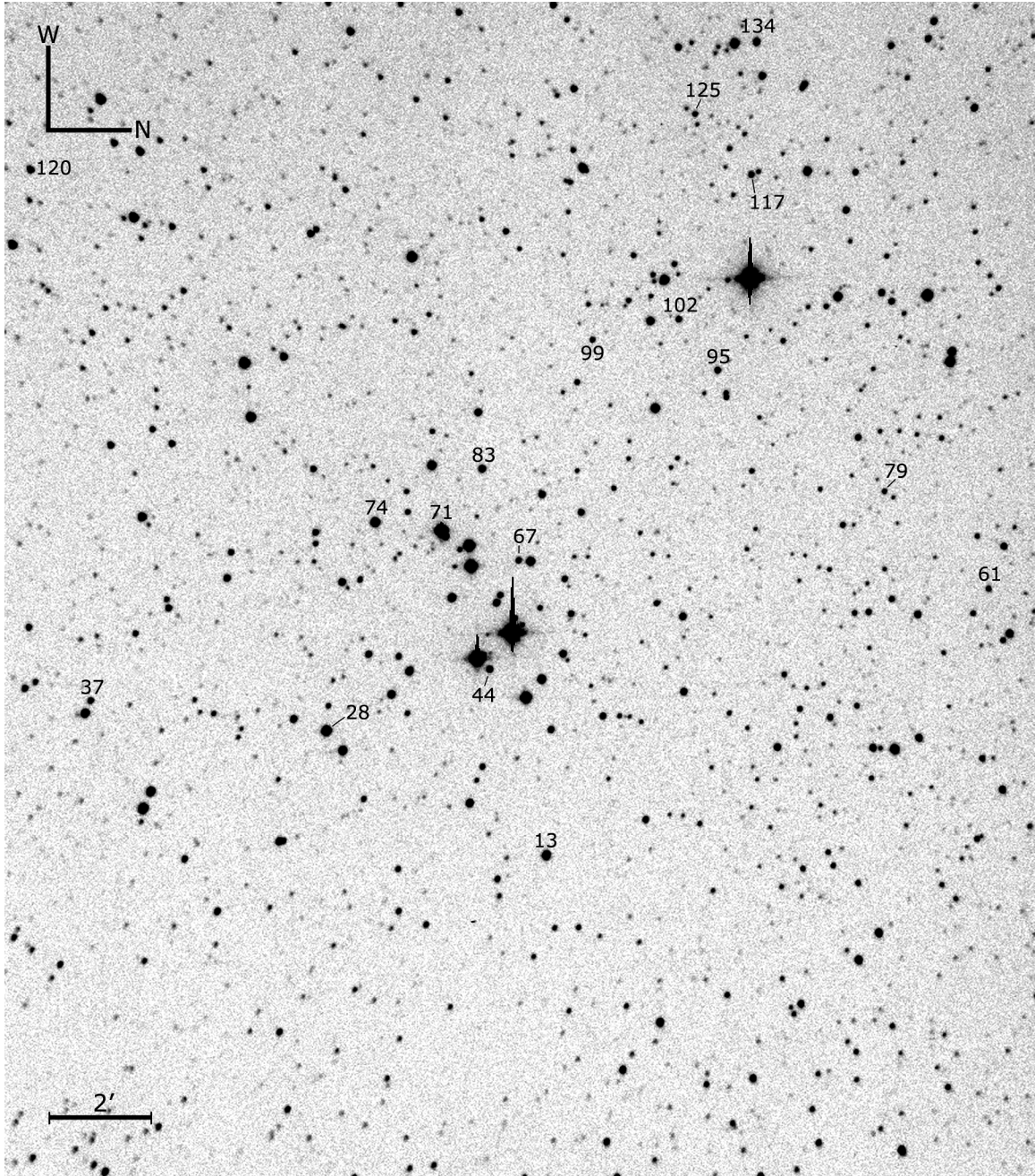


Figure 4.14: A finder chart for potential variables found in the field of NGC 7160. This image was taken on November 03, 2004 at OPO with the Apogee Ap47p CCD camera.

4.3 Time-series Plots

Time-series plots of the observational data, also referred to as light curves, were generated for each star with a RoMS value ≥ 0.9 , which resulted in hundreds of graphs. Although each were important for determining variability, only those stars which exhibited periodic variability are presented below. All of the time-series data were produced with PSF and differential photometry (see §§ 3.1.2 and § 3.2) where extreme care was taken to ensure that all atmospheric and instrumental effects were removed, and that any luminosity oscillations in the resulting data are solely from the observed object and random noise. In addition, the time (normally shown by Heliocentric Julian Date) in the time-series plots was adjusted so that the first image occurs at time zero with subsequent frames at increasing intervals of time (in units of hours). Only the data with time-frames greater than 1 hour are presented.

In the field of NGC 225

Four of the twenty-one potential variable stars found in the field of NGC 225 were selected for inclusion in this section. Figure 4.15 shows the time-series data for star 35 over two adjacent nights. Unfortunately, neither of the nights were long enough to include one full cycle of oscillation. However, the data includes one maximum on each night which suggests periodic variability. In addition, the maxima appear to occur at the same luminosity, which suggests that there is no zero point offset between the two nights of data. Further observations of star 35 are required in order to perform a period analysis.

The next three stars (42, 66, and 68) appear to exhibit similar trends in brightness over time, which are shown in Figures 4.16, 4.17, and 4.18, respectively. All of the stars exhibit some change in luminosity during each night with an unusual offset from night to night. This offset doesn't appear in any of the non-variable stars or in star 35, which suggests that these stars may be long period variables. Further observations of these stars are also required.

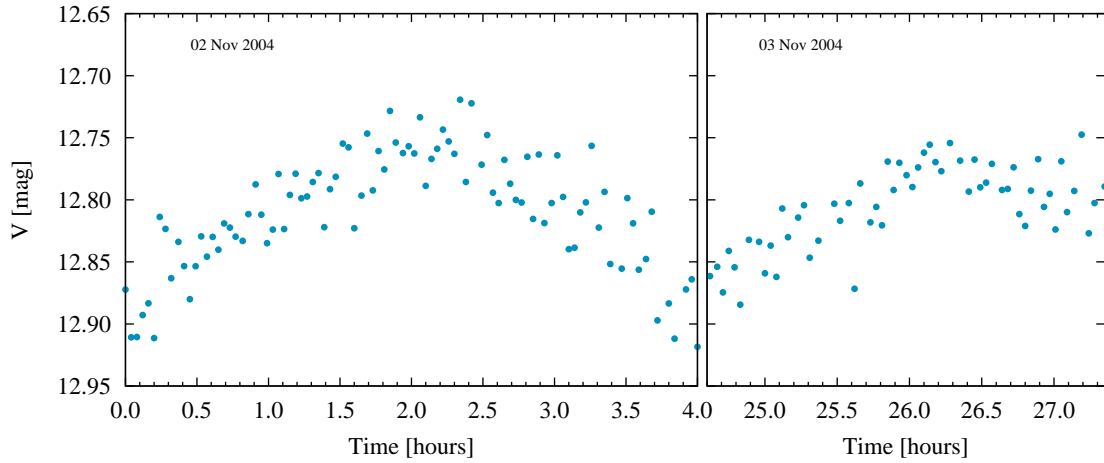


Figure 4.15: A time-series plot of the new variable star 35 in NGC 225. The adjacent nights were able to catch two maxima; however, further observations are required in order to determine a period and amplitude, and to ascertain whether the star is a δ Scuti pulsator.

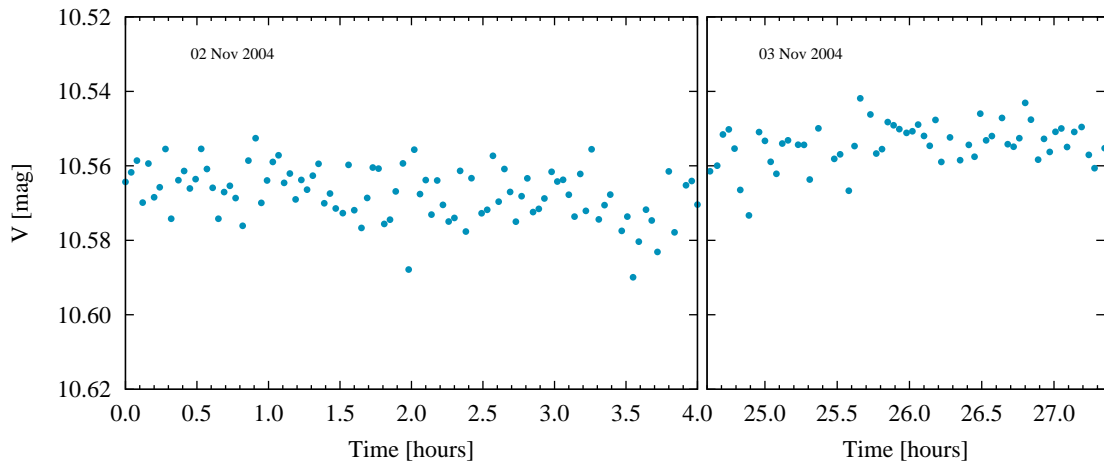


Figure 4.16: A time-series plot of the potential variable star 42 in NGC 225. This star exhibits very low-amplitude variability during each night and an unusual offset from night to night. This is perhaps a long period variable.

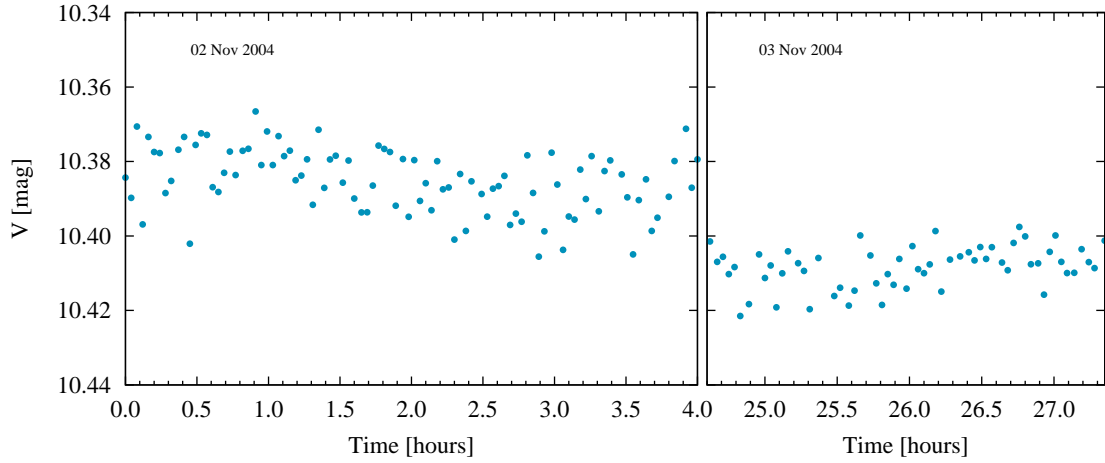


Figure 4.17: A time-series plot of the potential variable star 66 in NGC 225. This star shows some low-amplitude variability each night and a large offset in luminosity between nights.

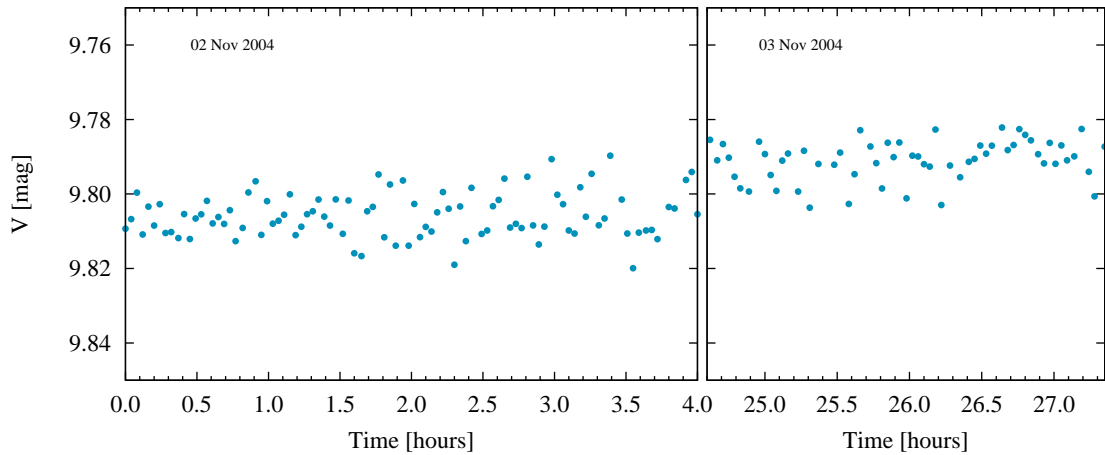


Figure 4.18: A time-series plot of the potential variable star 68 in NGC 225. This star displays an increase in luminosity from night to night, which suggests a long period.

In the field of NGC 559

Due to the short timescales of the data sets for NGC 559, which are on the order of half an hour, no time-series plots of the potential variable stars are presented. While applying the RoMS to the data, it was discovered that the time frames should be no shorter than a few hours, and for the best results the data sets should span ≥ 4 hours. Therefore, further observations of NGC 559 are required to determine if the new variables exhibit periodic oscillations in luminosity.

In the field of NGC 6811

Five of the seventeen potential variable star candidates found in NGC 6811 are presented. The gaps that appear in the data are the result of acquiring standards and extinction stars throughout the night. Figure 4.19 shows the periodic variability of star 8 (filled circles) as well as a comparison star from the ensemble, star 7 (open circles). The slight dip in the both sets of data, near 0.5 hours, suggests that such a variation is the result of the ensemble and not representative of the actual measured light from the stars of interest. The source of this dip is unknown at this time.

Star 30 is of particular interest because of the large spike in luminosity near the end of the night, as shown in Figure 4.20. A similar but slightly different pattern is exhibited by star 62 (see Figure 4.21). Upon initial inspection it was assumed that these spikes were caused by an eclipsing variable in the comparison ensemble, thus special attention was made to ensure that the ensemble only contained stable or normal stars. The fluctuations in the data appear to be the result of the stars themselves and not from any instrumental effects. Further observations should provide more insight as to what is happening with these stars.

Star 35, as shown in Figure 4.22, exhibits what appears to be pulsational oscillation; however, the gaps in the data make it difficult to determine a period and amplitude at this time. Star 41, as shown in Figure 4.23, displays some unusual

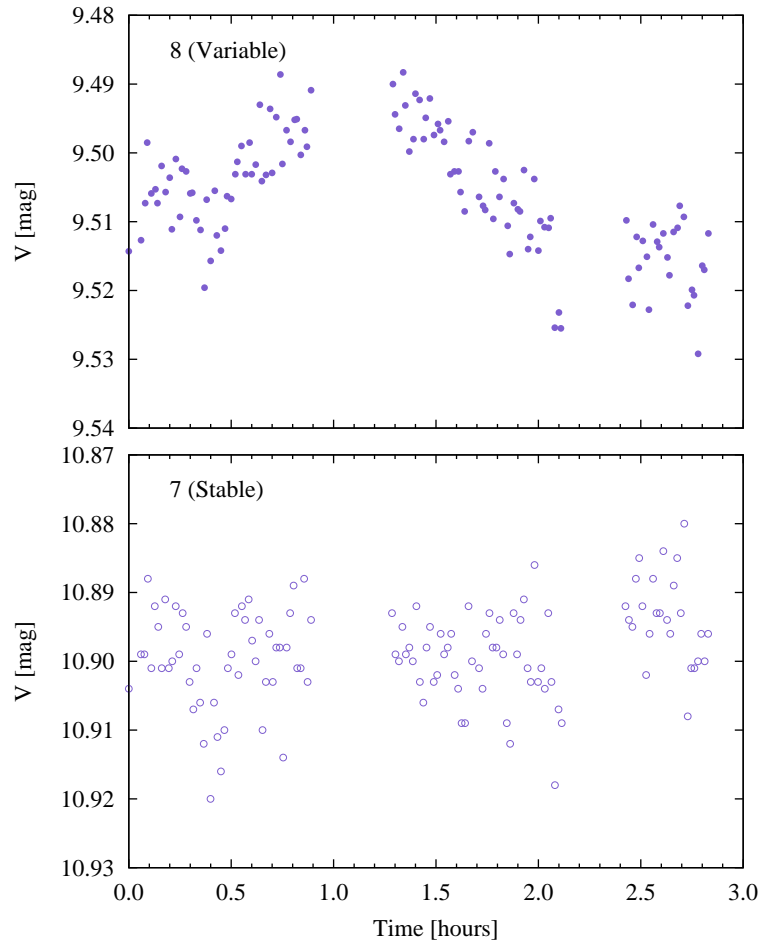


Figure 4.19: A time-series plot of the new variable star 8 (*top, filled circles*) and the nearby stable star 7 (*bottom, open circles*) in NGC 6811. The slight dip near 0.5 hours appears in the light curves of both stars and the ensemble. The source of such variation is unknown at this time.

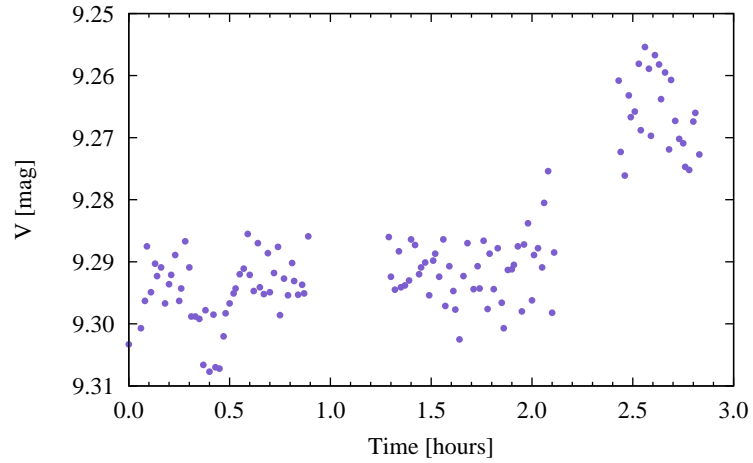


Figure 4.20: A time-series plot of the potential variable star 30 in NGC 6811. This star exhibits a particularly interesting pattern of variability that is not fully understood at this time.

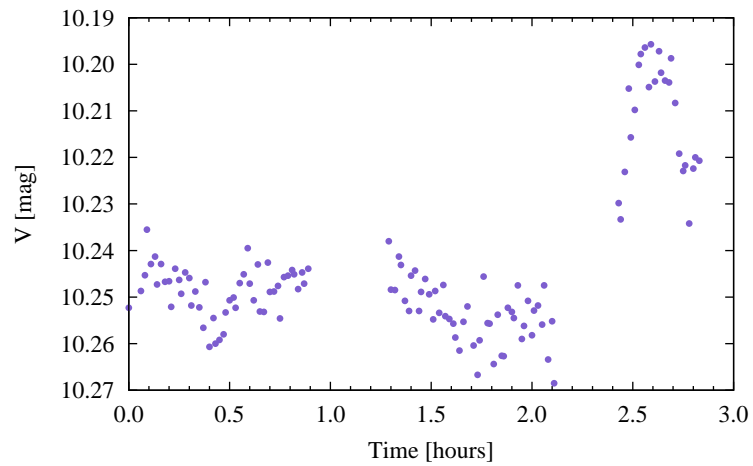


Figure 4.21: A time-series plot of the potential variable star 62 in NGC 6811. This star shows similar variability as star 30 but appears to be the result of the star itself.

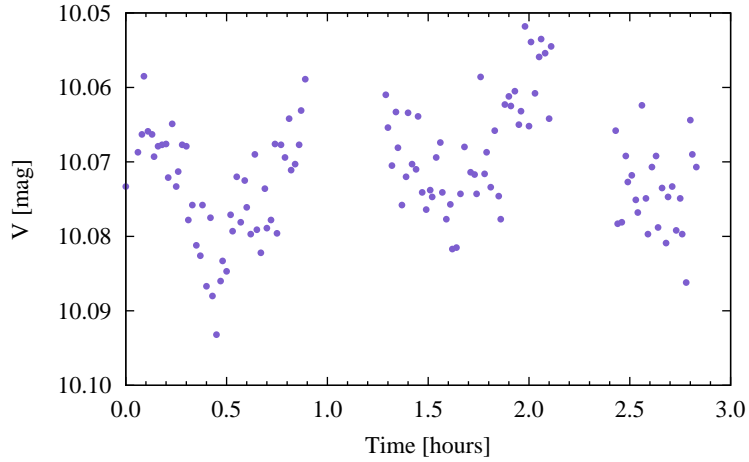


Figure 4.22: A time-series plot of the new variable star 35 in NGC 6811. This star appears to be a short period variable with a period on the order of an hour.

variability in its brightness. Further observations of both of these stars are required to determine the exact type of variability.

In the field of NGC 6940

The largest number of new variables were found in the field of NGC 6940, which are presented in the following graphs. Star 10 displays an interesting pattern in its light curve, which resembles that of an eclipsing variable (see Figure 4.24). Further observations are needed to determine the true nature of the exhibited variability. The remaining stars (32, 91, 99, 192, 198, 214, and 262) all exhibit pulsational variability in their time-series plots (see Figures 4.25 – 4.31). Stars 32, 91, 198, and 262 appear to be short period variables with periods on the order of a few hours, while stars 99, 192, and 214 have periods greater than three hours. Further observations of these stars are needed for a detailed period and amplitude analysis.

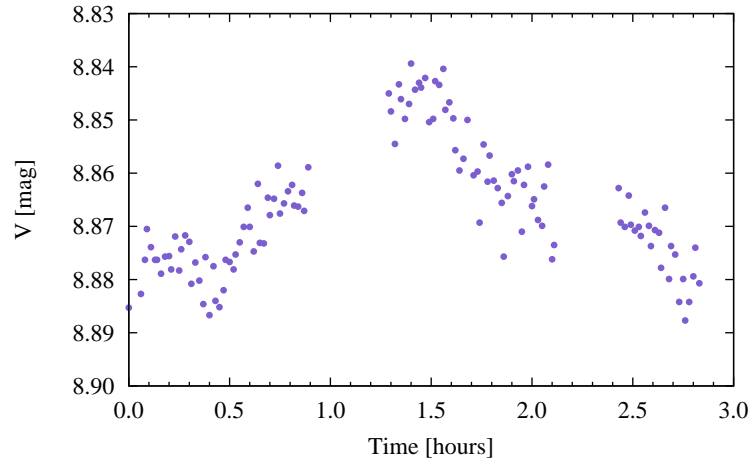


Figure 4.23: A time-series plot of the new variable star 41 in NGC 6811. The unusual variability present in this star is still not understood at this time. Further observations are required to determine type of variability.

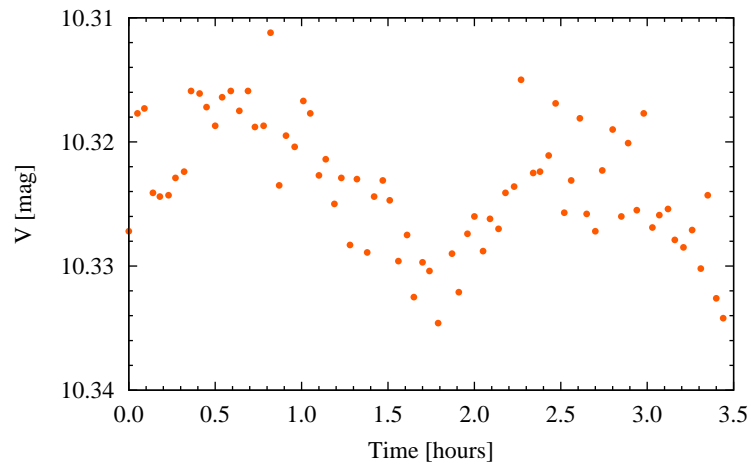


Figure 4.24: A time-series plot of the new variable star 10 in NGC 6940. The variability exhibited by this star resembles that of an eclipsing variable.

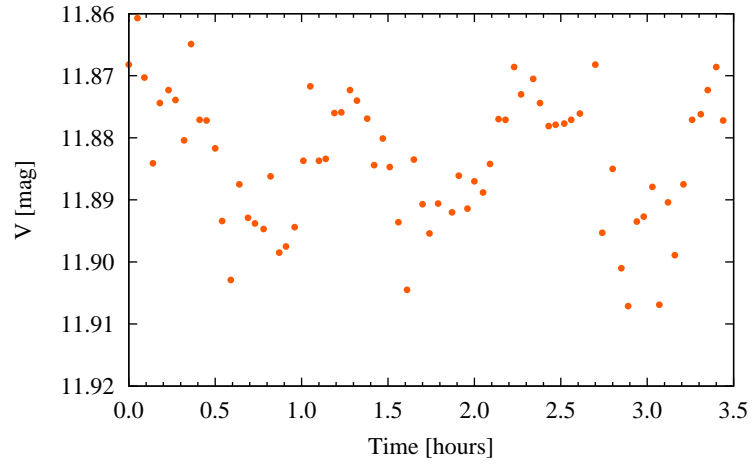


Figure 4.25: A time-series plot of the new variable star 32 in NGC 6940.

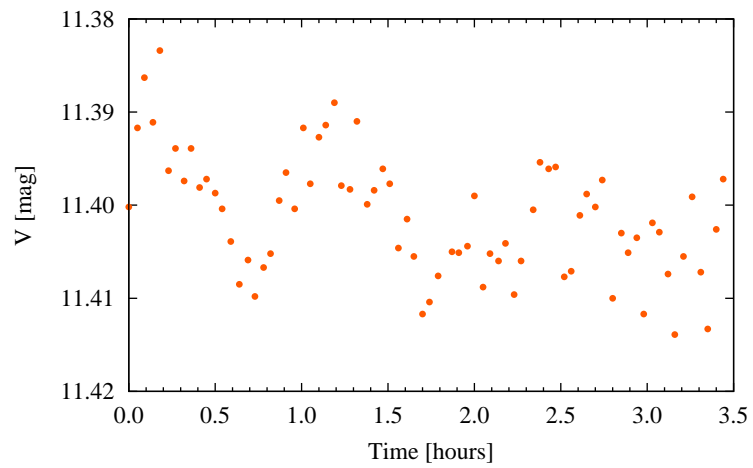


Figure 4.26: A time-series plot of the new variable star 91 in NGC 6940.

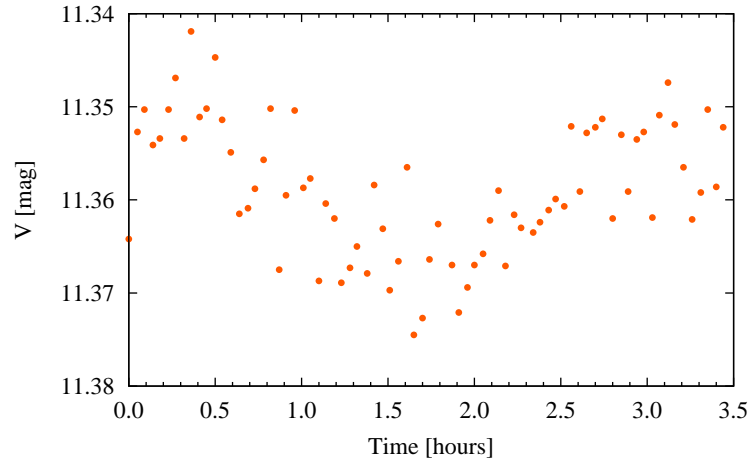


Figure 4.27: A time-series plot of the new variable star 99 in NGC 6940.

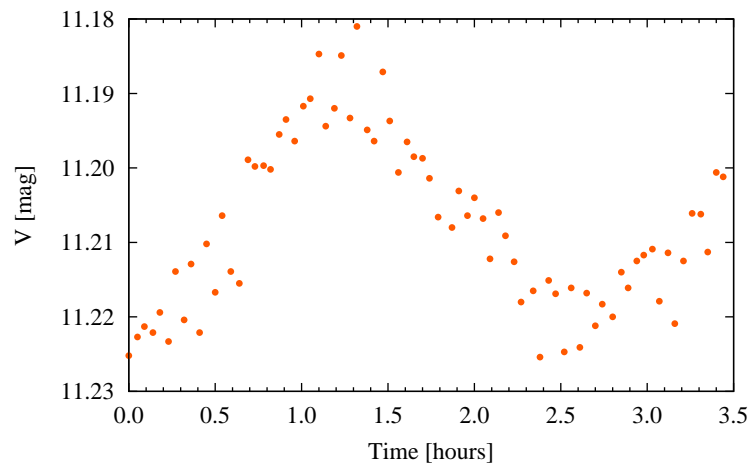


Figure 4.28: A time-series plot of the new variable star 192 in NGC 6940.

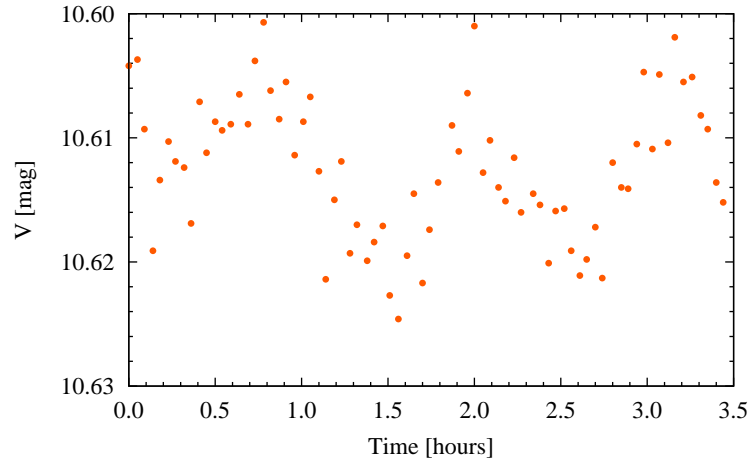


Figure 4.29: A time-series plot of the new variable star 198 in NGC 6940.

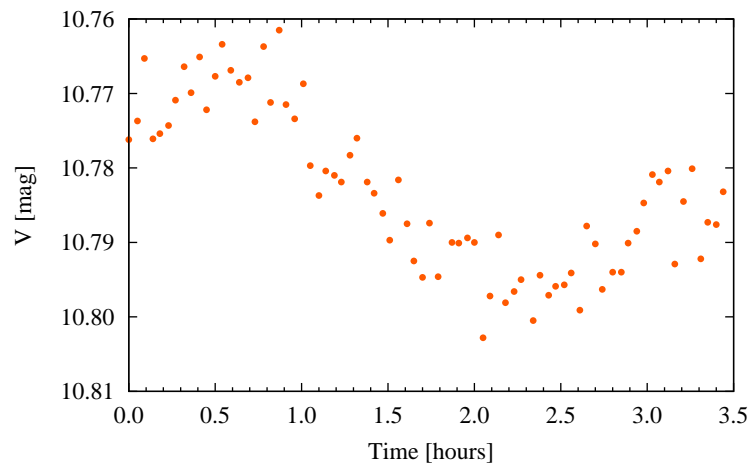


Figure 4.30: A time-series plot of the new variable star 214 in NGC 6940.

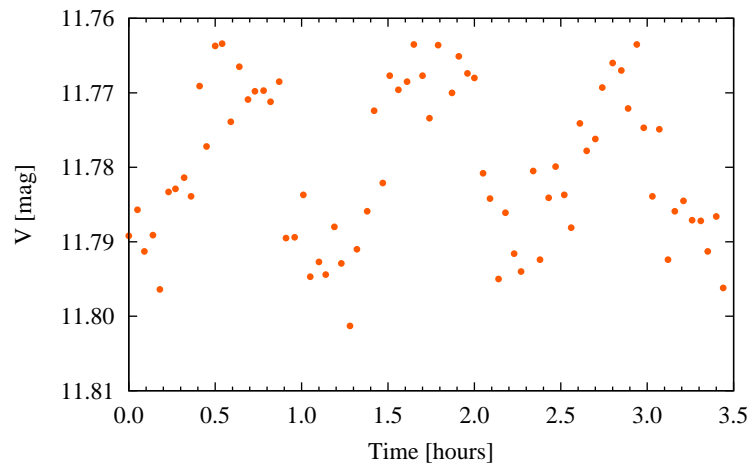


Figure 4.31: A time-series plot of the new variable star 262 in NGC 6940.

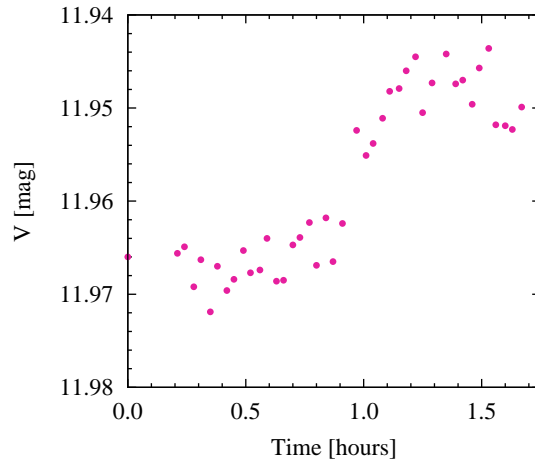


Figure 4.32: A time-series plot of the new variable star 34 in NGC 7142.

In the field of NGC 7142

Only one of the twenty-one potential variable star candidates found in the field of NGC 7142 is presented. Figure 4.32 shows the time-series data for star 34, which includes a minimum and maximum in a single night of data. Further observations of this star are required for a period and amplitude analysis.

In the field of NGC 7160

Seventeen suspected variables were found in the field of NGC 7160; however, none of them exhibited a recognizable, periodic pattern. As a result, no time-series plots are presented at this time. Further observations of NGC 7160 are required to determine if the suspected variables are indeed variable or just noisy stars.

Chapter 5

Conclusions

Astronomy has been and always will be in the pursuit of greater precision, as well as pushing the limits of what can be detected and measured. This thesis examined the methods for obtaining accurate photometric measurements of stellar objects using PSF fitting, correcting photometric measurements for atmospheric extinction and variable seeing with high-precision differential photometry, and detecting new variable stars with the RoMS. The development of two new computer programs, CLUSTER and ROMS, has provided a nearly-automated system for performing high-precision differential photometry and applying the RoMS to large data sets.

The goal of this research was to apply the RoMS to observational data of the clusters NGC 225, NGC 559, NGC 6811, NGC 6940, NGC 7142, and NGC 7160. The RoMS value distributions were presented in histogram form, where the non-variable distributions were found near a RoMS value of 0.9. In addition, the variable star distributions were found predominantly above a RoMS value of 1.0, only a handful of which were found below 1.0. As a result, it was concluded that the percentage of variables found with RoMS values between 0.8 and 1.0 is not 50%, as suggested by Hintz & Rose (2005), but appears to be unique for each cluster. Twenty-two new variables and eighty-seven suspected variable stars were discovered with the RoMS method, and time-series data of the new variables were presented in graphical form. Further observations of the new variables are needed for period and amplitude analysis, while more data is needed to confirm variability among the suspected variables.

Plans for the Future

The methods and programs presented in this thesis form the base or foundation for future study of additional open clusters and detection of low-amplitude variable

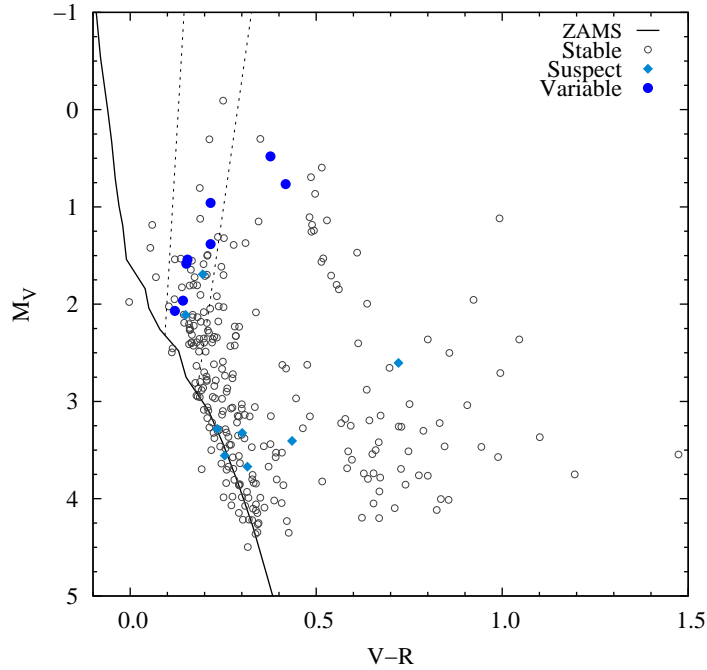


Figure 5.1: A CM-diagram of NGC 6940, with the classical instability strip. This figure shows that the variables (filled circles) are primarily located within the instability strip, which is where we would expect them.

stars at Brigham Young University. Some anticipated projects include proper calibration of colors and magnitudes of the stars in the cluster fields, and generating CM-diagrams (see Figure 5.1) to find the locations of the new variables in relation to the instability strip. Figure 5.1 is an example of a calibrated CM-diagram of a cluster, with the classical instability strip. Other prospective work will involve applying the RoMS method to larger runs of data in search of long and short period variables, and exploring the relationship between the error and the detectable amplitude limit of variable stars for ground-based telescopes.

Appendix A

User's Guide to CLUSTER

CLUSTER is a procedural program, written in C, that originated as an expansion of the program VARSTAR5, which was written by Eric Hintz. VARSTAR5 was designed to perform differential photometry on small groups of stars (≤ 25) and on known variable stars. When working with a handful of stars, VARSTAR5 is able to accomplish the task quickly and efficiently. However, several problems arose when VARSTAR5 was applied to a large number of stars (i.e. hundreds of stars), and when the variables were not known before hand. Although these problems are not discussed here, they were the motivation behind the development and creation of CLUSTER.

A.1 Expected Input File

The user is expected to provide a data file (often referred to as a .lst file) that consists of five, space-delimited columns of the following information: the star's ID number, the instrumental magnitude, the observation time or Heliocentric Julian Date (HJD), the air mass, and the passband filter. For IRAF users, the file is generated using the IRAF command, `txdump`, whereas DAOPHOT users should use the `make1st.sh` script provided by Maxwell (2004). An example of the full `txdump` command is

```
txdump N6940*.mag.1 id,mag,otime,xairmass,ifilter yes > N6940.lst
```

where `N6940*.mag.1` are the text files whose fields (`id`, `mag`, `otime`, `xairmass`, `ifilter`) are to be printed to the file `N6940.lst`. It is important to note that at this time CLUSTER cannot handle INDEF values in the input file, and can handle only one passband filter at a time. As a result, the user should check the input file for INDEF values before running CLUSTER. Also, separate data files should be created

Figure A.1: A sample input file for CLUSTER.

```
=====
  1 11.188 2453229.67380083 1.19872 V
  2 13.712 2453229.67380083 1.19872 V
  3 14.219 2453229.67380083 1.19872 V
  4 13.250 2453229.67380083 1.19872 V
  5 11.260 2453229.67380083 1.19872 V
  6 13.046 2453229.67380083 1.19872 V
  7 13.516 2453229.67380083 1.19872 V
  8 12.528 2453229.67380083 1.19872 V
  9 12.487 2453229.67380083 1.19872 V
 10 10.378 2453229.67380083 1.19872 V
      .
      .
      .
=====
(1) (2) (3) (4) (5)
```

- (1) Star's ID number.
- (2) The instrumental magnitude, measured from PSF fitting or aperture photometry.
- (3) HJD of the observation.
- (4) The air mass of the observation.
- (5) The passband filter through which the observation was made.

for each filter. Figure A.1 shows a sample input file for CLUSTER in the proper format.

A.2 A Typical Run of CLUSTER

In order to run CLUSTER, the user is required to give the filename for the input file as well as the filenames for each of the three output files. An example of the full command is as follows:

```
cluster5 N6940.lst N6940R1.err N6940R1.mag N6940R1.log
```

where `cluster5` is the most recent version of CLUSTER, `N6940.1st` is the input data filename, `N6940R1.err` is the error filename, `N6940F1.mag` is the magnitude filename, and `N6940R1.log` is the log filename. If any of the filenames are omitted by the user, then a help message is printed to the screen.

At the beginning of the program, the user is prompted for the star ID numbers of any known variable stars. These numbers are saved and always removed from the ensemble. This feature may also be used to remove other stars that may have drifted off the frame and/or stars that are located well above the error curve in the ME-diagram. It is important to note that the user is only prompted at the beginning of the program.

Once the known variable stars have been entered, CLUSTER will prompt the user for the cut value. All stars with standard errors greater than the cut value are then removed from the ensemble. Due to time constraints this feature has not been removed from the program, however, it has been found that removing stars based solely on their standard error is not the most effective method. Instead, the user should use the remove variable feature at the beginning of the program to remove all stars that are well above the error curve in the ME-diagram, then select a cut value high enough so that no other stars are removed from the ensemble. After the cut value has been applied, the user has the option of using another cut value or have CLUSTER write the appropriate output files.

A.3 Output Files

Three separate output files are created by CLUSTER, which include an *error file*, a *magnitude file*, and a *log file*. The primary purpose of the error file is to provide the user with the mean magnitude and standard error for each star, so that a ME-diagram may be generated easily. Figure A.2 presents a sample error file from CLUSTER along with an explanation of each column of data. The error file is ready to be plotted in Gnuplot.

Figure A.2: A sample error file from CLUSTER.

```
=====
  1 11.1353 0.00501
  2 13.6584 0.02634
  3 14.0753 0.03661
  4 13.1769 0.01957
  5 11.2055 0.00516
  6 13.0208 0.01643
  7 13.5236 0.02469
  8 12.4762 0.01032
  9 12.4420 0.01432
 10 10.3235 0.00531
    .
    .
    .
=====
(1)  (2)  (3)
```

- (1) Star ID number.
- (2) Star's mean magnitude, which is determined after differential photometry has been performed on the data.
- (3) Estimated standard error of the star's magnitude, which is determined after differential photometry has been performed on the data.

The second output file from CLUSTER is the magnitude file, as shown in Figure A.3, which provides the differential corrected magnitude for each star for each frame and the corresponding observation time or HJD. The magnitude file contains the complete set of data for all of the stars, unlike VARSTAR5 which outputs separate files for each star. This is done so that the user's directory isn't filled with hundreds of files for one run through CLUSTER; however, the user will have to cut and paste the data for a particular star before the data can be plotted in Gnuplot. It is important to note that the magnitude file is ready for use as the input file for the RoMS program.

The last output file from CLUSTER is the log file, as shown in Figure A.4, which provides the differential corrected value that was applied to all of the stars

Figure A.3: A sample magnitude file from CLUSTER.

```
=====
  1 11.14127 2453229.67380
  1 11.12552 2453229.67569
  1 11.13620 2453229.67757
  1 11.13341 2453229.67947
    .
    .
    .
 278 10.98627 2453229.67380
 278 10.99052 2453229.67569
 278 10.98420 2453229.67757
 278 10.98841 2453229.67947
    .
    .
    .
=====
(1)   (2)   (3)
```

- (1) Star ID number.
- (2) Star's magnitude, measured in magnitudes relative to the magnitude of the ensemble pseudo star.
- (3) HJD of the observation that corresponds to the star's magnitude.

on each frame. These values when plotted represent the atmospheric extinction and variable seeing throughout the night. In addition, the log file includes a list of the star ID numbers with corresponding markers that designate whether the star was removed from the ensemble by the cut value (*), selected as a variable star by the user (*v), while stars without a marker were included in the ensemble.

Figure A.4: A sample log file from CLUSTER.

```
=====
-0.05076
-0.04627
-0.03672
-0.02795
-0.02561
.
.
.
1   *
2   *
3   *
4
5
6
7
8
9   *v
10  *v
.
.
.
=====
(1)
(2) (3)
```

- (1) Ensemble correction for each image frame, which is added to every star on the frame to correct for atmospheric extinction and variable seeing.
- (2) Star's ID number.
- (3) Designates whether the star was removed from the ensemble by the cut value (*), selected as a variable star (*v), and included in the ensemble (nothing).

Appendix B

User's Guide to ROMS

Application of the RoMS by hand was found to be a tedious and overwhelming process, thus a procedural program, called ROMS, was written for the purpose of automating the application of the RoMS to a large data set for a cluster of stars. ROMS uses the unaltered magnitude file from CLUSTER as the input file (see § A.1), prompts the user for the coefficients (b_0 , b_1 , c_0 , and c_1) as defined by the analytical function (see § 3.3.2), prompts for the intercept or boundary value, x_1 , that separates the two pieces of the analytical function (see Eq. 3.5), and then applies the RoMS to the data as explained in § 3.3.1. Figure B.1 shows a sample output file from ROMS.

Figure B.1: A sample RoMS output file.

```
=====
 1 1.02041
 2 0.84492
 3 0.86922
 4 0.96101
 5 1.01623
 6 0.91827
 7 0.93292
 8 0.88097
 9 1.31172
10 1.13140
   .
   .
   .
=====
```

(1) (2)

- (1) Star's ID number.
- (2) RoMS value.

References

- Becker, W. & Fenkart, R. 1971, *A&AS*, 4, 241
- Bessell, M. S. 1990, *PASP*, 102, 1181
- Binney, J. & Merrifield, M. 1998, “Galactic Astronomy” (Princeton, NJ: Princeton University Press)
- Breger, M. 2000, *ASPC*, 210, 3B
- Buonanno, R., Corsi, C. E., Buzzoni, A., Cacciari, C., Ferraro, F. R., & Fusi Pecci, F. 1994, *A&A*, 290, 69
- Cacciari, C. & Clementini, G. 1990, *ASPC*, 11, C
- Carroll, B. W. & Ostlie, D. A. 1996, “Modern Astrophysics” (Addison-Wesley Publishing Company, Inc.)
- Chaboyer, B., Demarque, P., Kernan, P. J., & Krauss, L. M. 1998, *ApJ*, 494, 96
- Dachs, J. & Kaiser, D. 1984, *A&AS*, 58, 411
- Demarque, P., Woo, J., Kim, Y., & Yi, S. 2004, *ApJS*, 155, 667
- Enoch, M. L., Brown, M. E., & Burgasser, A. J. 2003, *AJ*, 126, 1006
- Friel, E. D. 1995, *ARA&A*, 33, 381
- Gautschy, A. & Saio, H. 1995, *ARA&A*, 33, 75
- Gautschy, A. & Saio, H. 1996, *ARA&A*, 34, 551
- Gilliland, R. L. 1992, *ASPC*, 23, 68
- Hintz, E. G. 2004, private communications

- Hintz, E. G. & Rose, M. B. 2005, PASP, 117, 955
- Hoag, A. A., Johnson, H. L., Iriarte, B., Mitchell, R. I., Hallam, K. L., & Sharpless, S. 1961, PUSNO, 17, 347
- Howell, S. 2000, "A Handbook of CCD Astronomy" (New York, NY: Cambridge University Press)
- Kafka, S. & Honeycutt, K. 2006, NOAO/AURA/NSF/WIYN
- Kerr, F. J. & Lynden-Bell, D. 1986, MNRAS, 221, 1023
- Lada et al. 1991, ApJ, 371, 171
- Lindoff, U. 1969, Arkiv För Astronomi, 5, 13
- Lindoff, U. 1972, A&A, 16, 315
- Maxwell, J. E. 2004, Thesis, Brigham Young University
- McNamara, D. H., Rose, M. B., Brown, P. J., Ketcheson, D. I., Maxwell, J. E., Smith, K. M., & Wooley, R. C. 2004, ASPC, 310, 525
- Merrifield, M. 1992, AJ, 103, 1442
- Paunzen, E., Zwintz, K., Maitzen, H. M., Pintado, O. I., & Rode-Paunzen, M. 2004, A&A, 418, 99
- Ponomareva, G. A. 1983, Trudy Gosud. Astr. Inst. Shterneberga LIII, 29
- Sagar, R. & Cannon, R. D. 1995, A&AS, 111, 75
- Samus et al. 2002, AZh, 29, 7, 532
- Schmidt-Kaler, T. 1982, Landolt-Börnstein New Series, group VI, 2b, 453
- SIMBAD database 2006, (<http://simbad.harvard.edu/cgi-bin/WSimbad.pl>)

Stetson, P. B. 1987, PASP, 99, 191

Stetson, P. B. 1990, PASP, 102, 932

Stetson, P. B. 1991, JRASC, 86, 71

Trumpler, R. J. 1930, Lick Obs. Bull., 14, 154

van den Bergh, S. & Heeringa, R. 1970, A&A, 9, 209

Warner, P. B., Kaye, A. B., & Guzik, J. A. 2003, ApJ, 593, 1049

WEBDA database 2006, (<http://www.univie.ac.at/webda/>)

Woodland, O. L. 2006, Senior Thesis, Brigham Young University